Allosteric stabilization of calcium and phosphoinositide dual binding engages three synaptotagmins in fast exocytosis

Janus R. L. Kobbersmed[1,2]*, Manon M. M. Berns[2,3]*, Susanne Ditlevsen[1], Jakob B. Sørensen[2] and Alexander M. Walter[2,3]

[1]Department of Mathematical Sciences, University of Copenhagen, Copenhagen, Denmark

[2]Department of Neuroscience, University of Copenhagen, Copenhagen, Denmark

[3]Molecular and Theoretical Neuroscience, Leibniz-Institut für Molekulare Pharmakologie, FMP im CharitéCrossOver, Berlin, Germany

*: equal contribution

For correspondence:

awalter@sund.ku.dk

Abstract

Synaptic communication relies on the fusion of synaptic vesicles with the plasma membrane, which leads to neurotransmitter release. This exocytosis is triggered by brief and local elevations of intracellular Ca^{2+} with remarkably high sensitivity. How this is molecularly achieved is unknown. While synaptotagmins confer the Ca^{2+} sensitivity of neurotransmitter exocytosis, biochemical measurements reported Ca^{2+} affinities too low to account for synaptic function. However, synaptotagmin's Ca^{2+} affinity increases upon binding the plasma membrane phospholipid $PI(4,5)P_2$ and, vice versa, Ca^{2+}-binding increases synaptotagmin's $PI(4,5)P_2$ affinity, indicating a stabilization of the $Ca^{2+}/PI(4,5)P_2$ dual-bound syt. We here devise a molecular exocytosis model based on this positive allosteric stabilization and the assumptions that (1.) synaptotagmin $Ca^{2+}/PI(4,5)P_2$ dual binding lowers the energy barrier for vesicle fusion and that (2.) the effect of multiple synaptotagmins on the energy barrier is additive. The model, which relies on biochemically measured $Ca^{2+}/PI(4,5)P_2$ affinities and protein copy numbers, reproduced the steep Ca^{2+} dependency of neurotransmitter release. Our results indicate that each synaptotagmin dual binding $Ca^{2+}/PI(4,5)P_2$ lowers the energy barrier for vesicle fusion by 4.85 k_BT and that allosteric stabilization of this state enables the synchronized engagement of three synaptotagmins for fast exocytosis. Furthermore, we show that mutations altering synaptotagmin's allosteric properties may show dominant-negative effects, even though synaptotagmins act independently on the energy barrier, and that dynamic changes of local $PI(4,5)P_2$ (e.g. upon vesicle movement) dramatically impact synaptic responses. We conclude that allosterically stabilized $Ca^{2+}/PI(4,5)P_2$ dual binding enables synaptotagmins to exert their coordinated function in neurotransmission.

Introduction

Regulated neurotransmitter (NT) release from presynaptic terminals is crucial for information transfer across chemical synapses. NT release is triggered by action potentials (APs), which are transient de- and repolarizations of the presynaptic membrane potential that induce Ca^{2+} influx through voltage-gated channels. The resulting brief and local elevations of the intracellular Ca^{2+} concentration ($[Ca^{2+}]_i$) trigger the fusion of NT-containing synaptic vesicles (SVs) from the so-called readily releasable pool (RRP), whose SVs are localized (docked) at the plasma membrane and molecularly matured (primed) for fusion (Kaeser and Regehr, 2017; Sudhof, 2013; Verhage and Sørensen, 2008). A high Ca^{2+} sensitivity of NT release is needed to achieve fast responses to the very short AP-induced Ca^{2+} transient and correspondingly, the SV fusion rate depends on the $[Ca^{2+}]_i$ to the 4th-5th power (Bollmann et al., 2000; Burgalossi et al., 2010; Heidelberger et al., 1994; Schneggenburger and Neher, 2000). Accordingly, previous models of NT release have assumed the successive binding of five Ca^{2+} ions to a sensor that regulates release (Bollmann *et al.*, 2000; Lou et al., 2005; Schneggenburger and Neher, 2000). However, how these macroscopic properties arise from the molecular components involved in SV fusion is still unknown.

The energy for SV fusion is provided by the assembly of the neuronal SNARE complex, which consists of vesicular synaptobrevin/VAMP and plasma membrane bound SNAP25 and syntaxin proteins (Jahn and Fasshauer, 2012; Sudhof, 2013). Ca^{2+} sensitivity of SV fusion is conferred by the vesicular protein synaptotagmin (syt), which interacts with the SNAREs (Brewer et al., 2015; Littleton et al., 1993; Mohrmann et al., 2013; Schupp et al., 2016; Zhou et al., 2015; Zhou et al., 2017). Several syt isoforms are expressed in synapses. Depending on the synapse type (e.g. mouse hippocampal pyramidal neurons or the Calyx of Held), syt1 or syt2 is required for synchronous, Ca^{2+}-induced fusion (Geppert et al., 1994; Kochubey et al., 2016; Kochubey and Schneggenburger, 2011; Sudhof, 2013). These two syt isoforms are highly homologous and contain two cytosolic, Ca^{2+}-binding domains, C2A and C2B (Sudhof, 2002), of which the C2B domain has been shown to be essential, and in some cases even sufficient, for synchronous NT release (Bacaj et al., 2013; Gruget et al., 2020; Kochubey and Schneggenburger, 2011; Lee et al., 2013; Mackler et al., 2002). The C2B domain contains two Ca^{2+} binding sites on its top loops (Fernandez et al., 2001). In addition, a second binding site allows the C2B domain to bind to the signaling lipid phosphatidylinositol 4,5-phosphate ($PI(4,5)P_2$) located in the plasma membrane (Bai et al., 2004; Fernandez-Chacon et al., 2001; Honigmann et al., 2013; Li et al., 2006; Xue et al., 2008), but might also participate in (possibly transient) SNARE interactions (Brewer *et al.*, 2015; Zhou *et al.*, 2015; Zhou *et al.*, 2017). A third site, located in the far end of the C2B domain (R398 and R399 in mouse syt1), is also involved in both SNARE- and membrane contacts (Nyenhuis et al., 2021; Xue *et al.*, 2008; Zhou *et al.*, 2015). Via these interactions, the syt C2B domain can induce

close membrane-membrane contact *in vitro* (Araç et al., 2006; Chang et al., 2018; Honigmann *et al.*, 2013; Nyenhuis *et al.*, 2021; Seven et al., 2013; Xue *et al.*, 2008), stable vesicle-membrane docking (Chang *et al.*, 2018; Chen et al., 2021; de Wit et al., 2009), as well as dynamic vesicle-membrane association upon Ca^{2+} influx in the cell (Chang *et al.*, 2018).

Despite its central role as the Ca^{2+} sensor for NT release, the intrinsic Ca^{2+} affinity of the isolated syt C2B domain is remarkably low (KD ≈ 200 µM, (Radhakrishnan et al., 2009; van den Bogaart et al., 2012)), much lower than the Ca^{2+} sensitivity of NT release (Bollmann *et al.*, 2000; Schneggenburger and Neher, 2000). However, binding of the C2B domain to $PI(4,5)P_2$, which is enriched at synapses (van den Bogaart et al., 2011a), drastically increases its Ca^{2+} affinity (van den Bogaart *et al.*, 2012). Similarly, the affinity for $PI(4,5)P_2$ increases upon Ca^{2+} binding (Pérez-Lara et al., 2016; van den Bogaart *et al.*, 2012). This indicates a positive allosteric coupling between the binding sites for Ca^{2+} and $PI(4,5)P_2$, which promotes dual binding of $Ca^{2+}/PI(4,5)P_2$ (Li *et al.*, 2006; Radhakrishnan *et al.*, 2009; van den Bogaart *et al.*, 2012). As binding of both molecules to syt is involved in fusion (Kedar et al., 2015; Li *et al.*, 2006; Mackler *et al.*, 2002; Mackler and Reist, 2001; Wang et al., 2016; Wu et al., 2021a; Wu et al., 2021b), this positive allosteric coupling might be central to syt's function in triggering Ca^{2+} induced exocytosis (van den Bogaart *et al.*, 2012).

In this paper we developed a mathematical model in which the dual binding of the C2B domain to Ca^{2+} and $PI(4,5)P_2$ is promoting fusion. The model, which is based on the measured affinities and allostericity of Ca^{2+} and $PI(4,5)P_2$ binding, describes stochastic binding/unbinding reactions at the level of individual syts and stochastic SV fusion events. The model predicts that each C2B domain engaging in dual $Ca^{2+}/PI(4,5)P_2$ binding lowers the energy barrier for fusion by 4.85 k_BT. Three vesicular syts simultaneously engage their C2B domains in dual $Ca^{2+}/PI(4,5)P_2$ binding for fast NT release and this simultaneous engagement of multiple syts crucially relies on the positive allosteric coupling between Ca^{2+} and $PI(4,5)P_2$ binding. We explored consequences of putative mutants affecting $Ca^{2+}/PI(4,5)P_2$ binding and/or the allosteric coupling between the binding sites of both species and suggest that changes of the allostericity contribute to dominant negative effects. Moreover, dynamic changes of $PI(4,5)P_2$ accessibility for the syts (e.g. induced by SV movement to the plasma membrane) are predicted to dramatically impact synaptic responses. We conclude that allosterically stabilized $Ca^{2+}/PI(4,5)P_2$ dual binding to the C2B domains forms the molecular basis for synaptotagmins to exert their cooperative control of neurotransmitter release.

97 ## Results

98 **An experiment-based model of the triggering mechanism for SV fusion based on molecular**
99 **interactions between syt, Ca^{2+}, and $PI(4,5)P_2$**

100 To develop an experiment-based model of NT release based on molecular properties of syt, we first
101 described the reaction scheme of a single C2B domain. The C2B domain binds $PI(4,5)P_2$ and two Ca^{2+}
102 ions (Fernández-Chacón et al., 2002; Honigmann *et al.*, 2013; Mackler *et al.*, 2002; van den Bogaart *et*
103 *al.*, 2012; Xue *et al.*, 2008). Therefore, in our model the C2B domain can be in four different states
104 (Figure 1A): (1) an "empty" state, (2) a $PI(4,5)P_2$-bound state, (3) a state with two Ca^{2+} ions bound, and
105 (4) a "dual-bound" state in which the C2B simultaneously engages $Ca^{2+}/PI(4,5)P_2$ binding. The binding
106 affinities of syt1 C2B for Ca^{2+} and $PI(4,5)P_2$ were set to those measured *in vitro* ($K_{D,2Ca2+}$ and $K_{D,PIP2}$)(van
107 den Bogaart *et al.*, 2012). Binding of $PI(4,5)P_2$ to the C2B domain was shown to increase the domain's
108 affinity for Ca^{2+} and vice versa, indicating a positive allosteric coupling between the two binding sites
109 (van den Bogaart *et al.*, 2012). We therefore implemented a positive allosteric stabilization of the dual-
110 bound state in the model (illustrated by the red shaded areas of the C2B domain in Figure 1A) by
111 introducing the allosteric factor (A= 0.00022, see Methods (van den Bogaart *et al.*, 2012)) which slows
112 down the Ca^{2+} and $PI(4,5)P_2$ dissociation from the dual-bound state.

113 We next extended the model to the level of the complete SV. On average, SVs contain 15 copies
114 of syt1 (Figure 1B) (Takamori et al., 2006), which may work together to regulate SV fusion. Spontaneous
115 release occurs at low rates (with a rate constant 'L_+'), reflected by a high initial energy barrier for SV
116 fusion (Figure 1C). Because syt's stimulation of SV fusion likely relies on the simultaneous binding of
117 both Ca^{2+} and $PI(4,5)P_2$ (Kedar *et al.*, 2015; Li *et al.*, 2006; Mackler *et al.*, 2002; Mackler and Reist, 2001;
118 Wang *et al.*, 2016; Wu *et al.*, 2021a; Wu *et al.*, 2021b), we assumed that each dual-bound C2B domain
119 promotes exocytosis by lowering this barrier. How this might be achieved exactly is unknown, but could
120 involve bridging plasma and SV membranes (Figure 1A), changing the curvature of the plasma
121 membrane (Figure 1 – Figure supplement 1), changing the local electrostatic environment, or directly
122 or indirectly promoting SNARE complex assembly (Bhalla et al., 2006; Martens et al., 2007; Ruiter et
123 al., 2019; Schupp *et al.*, 2016; Tang et al., 2006; van den Bogaart et al., 2011b; Zhou *et al.*, 2015; Zhou
124 *et al.*, 2017). We assumed that multiple syts may progressively lower the energy barrier by the
125 successive engagement of their C2B domains in dual $Ca^{2+}/PI(4,5)P_2$ binding, and investigated the
126 simplest scenario, in which each dual-bound C2B domain contributed the same amount of energy (E_{syt})
127 thereby increasing the fusion rate by the same factor (f) (Figure 1C)(Schotten et al., 2015). The number
128 of syts that can simultaneously promote fusion may be limited by their access to $PI(4,5)P_2$ in the plasma

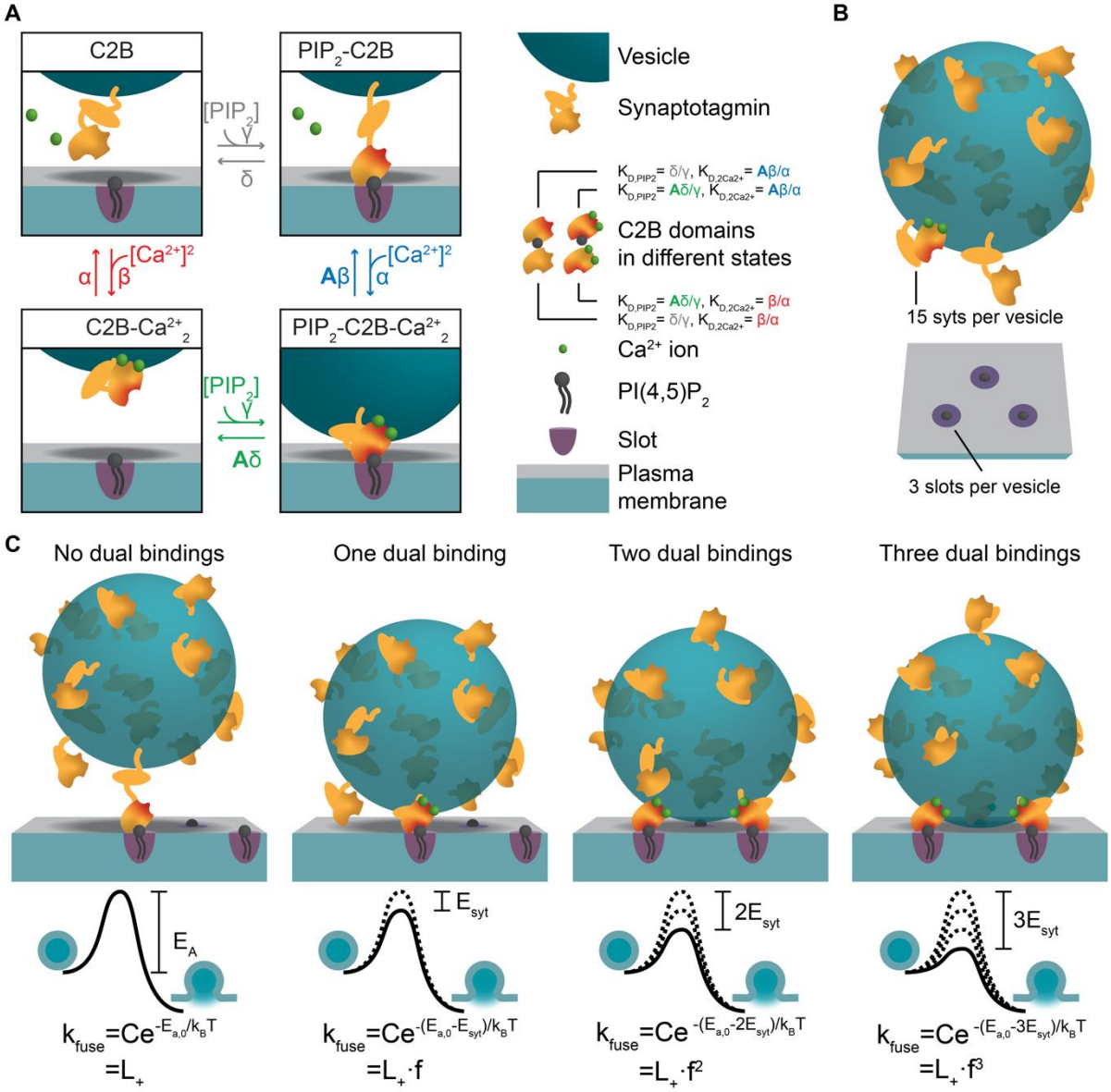

Figure 1: A molecular model of NT release triggered by Ca^{2+} and PI(4,5)P_2 binding to the syt1 C2B domain. A) The reaction scheme of a single syt C2B domain. Each syt can be in one of four binding states: Nothing bound (top left), PI(4,5)P_2 bound (top right), two Ca^{2+} ions bound (bottom left), and PI(4,5)P_2 and two Ca^{2+} ions bound (bottom right). Simultaneous binding of Ca^{2+} and PI(4,5)P_2 to the syt C2B domain is referred to as dual binding. The factor A<1 on the dissociation rates (β and δ) from the dual-bound state represents the positive allosteric effect of simultaneous PI(4,5)P_2 and Ca^{2+} binding and leads to stabilization of the dual-bound state. The ratio between dissociation rate and association rate constants (β/α and δ/γ) is equal to the respective dissociation constants of syt1 determined *in vitro* ($K_{D,2Ca2+}$ =221^2 μM^2 and $K_{D,PIP2}$ =20 μM, (van den Bogaart *et al.*, 2012)). An alternative reaction scheme where Ca^{2+} binding leads to association of the C2B domain with the plasma membrane is shown in Figure 1 – figure supplement 1. Our model is not influenced by the assumptions on whether Ca^{2+} binding to syt leads to plasma membrane or vesicle association. **B)** The stoichiometry at the SV fusion site. We assume 15 syts per SV (Takamori *et al.*, 2006), and that the association of the syt C2B domain to PI(4,5)P_2 is limited to a finite number of slots (here illustrated for M_{slots}=3). **C)** The effect of formation of multiple dual bindings on the energy barrier for SV fusion and the SV fusion rate. We assume that each dual-binding C2B domain lowers the energy barrier for fusion by the same amount (E_{syt}, illustrated in middle row), thereby increasing the fusion rate (k_{fuse}) with a factor *f* for each dual binding (equation in bottom row). The fusion rate for an SV with no dual bindings formed is set to L_+. The model is a Markov model, which can be summarized in a state diagram describing the reactions of the syt-harboring SV (Figure 1 – figure supplement 2).

148 membrane. This could be due to limited space beneath the SV or limited molecular access to bind
149 PI(4,5)P_2 clusters and/or SNAREs (de Wit *et al.*, 2009; Mohrmann *et al.*, 2013; Rickman and Davletov,
150 2003). We therefore created a model that stochastically describes the binding status of individual SVs
151 (Figure 1 – Figure supplement 2) with a limited number of PI(4,5)P_2 association possibilities ('slots')
152 and investigated how this number affects physiological responses.

153

154 **At least three PI(4,5)P_2 binding slots are required to reproduce release kinetics from the calyx of Held**
155 **synapse**

156 A hallmark of the NT release reaction is its large dynamic range in response to Ca^{2+} stimuli as
157 impressively demonstrated by experimental data from the calyx of Held synapse where release
158 latencies (defined as the time of the fifth SV fusion after the stimulus) and exocytosis rates have been
159 measured for a broad range of Ca^{2+} concentrations (using Ca^{2+} uncaging)(Bollmann *et al.*, 2000;
160 Kochubey and Schneggenburger, 2011; Lou *et al.*, 2005; Schneggenburger and Neher, 2000; Sun et al.,
161 2007). At this well-established model synapse, fast NT release is controlled by syt2, which is
162 functionally redundant with syt1 in neurons (Kochubey *et al.*, 2016; Xu et al., 2007).

163 We evaluated whether our model could reproduce this Ca^{2+} dependence by simulating release
164 latencies and peak release rates in response to step-like Ca^{2+} stimuli. The ability to reproduce the
165 experimental data depended on the number of 'slots' for syt PI(4,5)P_2 binding (Figure 2A). We first
166 fitted the free parameters in our model by optimizing the agreement (i.e. by reducing a pre-defined
167 cost function, see Methods) between model predictions and release rates and latencies determined
168 experimentally by Kochubey and Schneggenburger (Figure 2A)(Kochubey and Schneggenburger,
169 2011). During this fitting process, we took the entire distribution of the experimentally obtained
170 release latencies into account by using the likelihood function (see Methods). This was not feasible for
171 the experimental peak release rates (since accurate computation of the maximum rate of stochastic
172 events is not feasible), which were therefore compared to the closed form solution of the model (see
173 Methods). Because the affinities for Ca^{2+} and PI(4,5)P_2, and the allosteric coupling between both
174 species ($K_{D,2Ca2+}$, $K_{D,PIP2}$ and A, Figure 1A, Figure 1 – figure supplement 2) as well as the RRP size
175 (including its variance) were taken from literature (Table 1) (Figure 2 – figure supplement 1) (van den
176 Bogaart *et al.*, 2012; Wölfel and Schneggenburger, 2003), we only had to estimate five unknown
177 ("free") parameters: (1) the binding rate constant of the two Ca^{2+} ions (α), (2) the binding rate constant
178 of PI(4,5)P_2 (γ), (3) the PI(4,5)P_2 concentration ([PI(4,5)P_2]), (4) the reduction of the energy barrier for
179 fusion induced by Ca^{2+}/PI(4,5)P_2 dual binding of one C2B domain (E_{syt}) and (5) (like in previous models)
180 a fixed delay (d) between time of uncaging and response onset (see (Kochubey and Schneggenburger,

181 2011; Schneggenburger and Neher, 2000)). Having obtained the best fit parameters, peak release rates
182 and release latencies (Figure 2A) were stochastically simulated based on the closed-form solution of
183 the Markov model (see Methods).

184 We systematically varied the number of slots (M_{slots}) from one to six, optimized the free
185 parameters for each of these choices, and compared the best fit solutions. With a single slot (M_{slots} =1),
186 the model accounted for experimentally observed release latencies, but failed to reproduce the steep
187 relationship between $[Ca^{2+}]_i$ and peak release rates (Figure 2A). Adding more slots strongly improved
188 the agreement with experimental data. The best agreement was found with three slots (M_{slots}=3) and
189 the agreement slightly decreased with more slots (M_{slots} >3) (Figure 2B). However, all models with at
190 least three slots (M_{slots}≥3) captured the steep dependency of peak release rates on $[Ca^{2+}]_i$, with a
191 maximum slope of 4-5 on a double-logarithmic plot (Figure 2C) (Schneggenburger and Neher, 2000).

192 Our model made it possible to inspect the fate of each individual fusing SVs, including the
193 number of synaptotagmins dually binding Ca^{2+} and $PI(4,5)P_2$ just before fusion. Remarkably, even in
194 models with more than three slots (M_{slots}>3), fast NT release (for moderate to high $[Ca^{2+}]_i$) was
195 predicted to primarily engage three dual-bound syt C2B domains (while fewer dual-bound syts
196 mediated fusion for lower $[Ca^{2+}]_i$)(Figure 2D-E, Figure 2 - figure supplement 2, Figure 2 - figure
197 supplement 3). Correspondingly, the estimated reduction of the energy barrier for fusion by each
198 $Ca^{2+}/PI(4,5)P_2$ dual-binding C2B domain was similar (E_{syt}≈5 k_BT) for all versions of the model with at
199 least three slots (M_{slots}≥3) (Figure 2F, see Table 2 for other best fit model parameters). Manually forcing
200 a lower contribution to the energy barrier for fusion in a model with six slots and refitting the remaining
201 parameters, which would be required to involve more dual bindings in fusion, resulted in a too steep
202 dependence of the peak release rate vs. $[Ca^{2+}]_I$ (figure 2 – figure supplement 4). Thus, our model
203 predicts that three syts actively reduce the energy barrier for fast SV fusion. Consequently, we used
204 the model with three slots (M_{slots}=3) for further simulations.

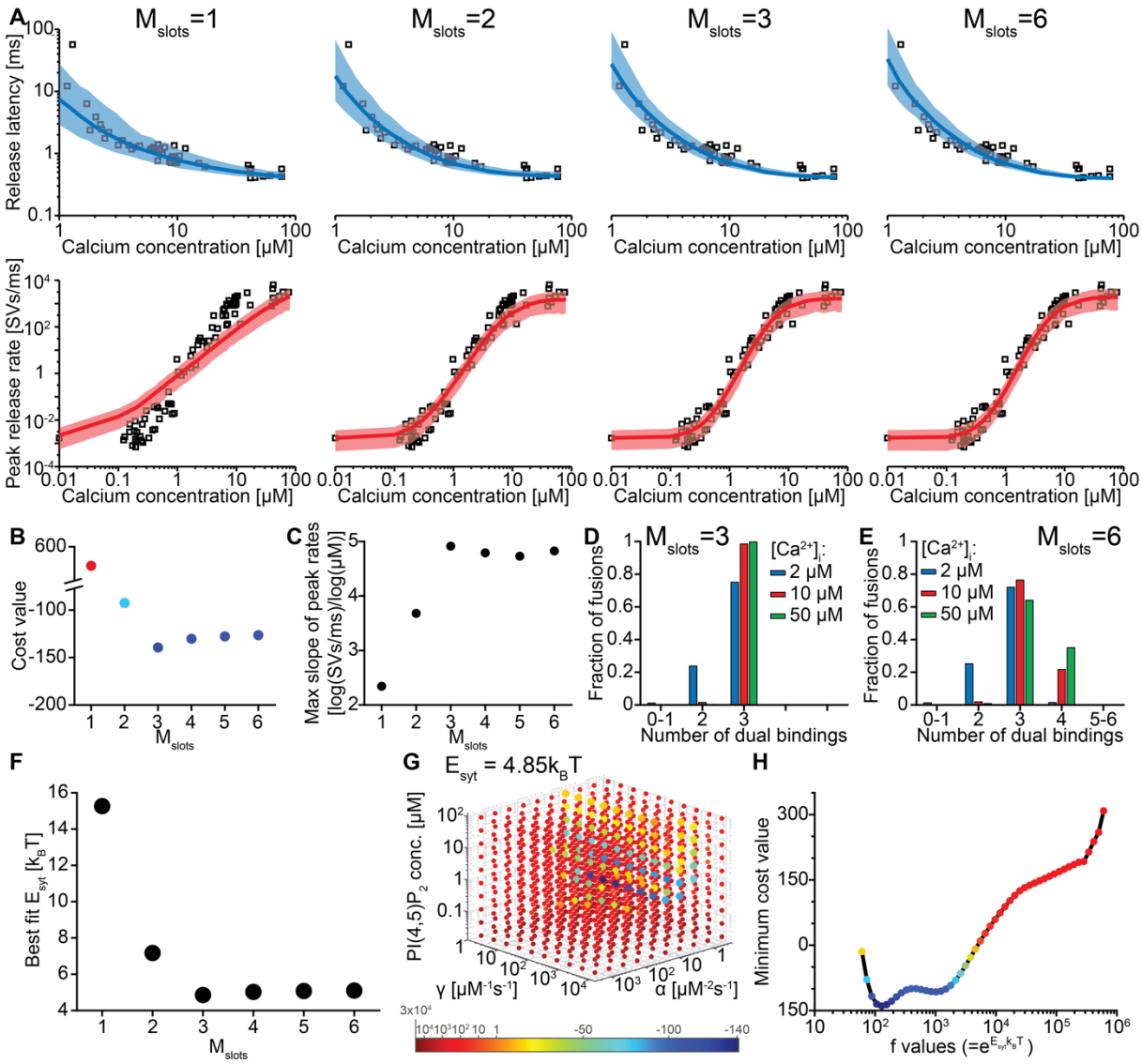

Figure 2: The model reproduces the Ca^{2+} dependency of SV fusion when at least three syts can simultaneously bind PI(4,5)P_2. A) Best fit results for different choices of M_{slots}. The top panels show best fit model prediction of the release latencies (time to fifth SV fusion), and the bottom panels show the predicted peak release rates at varying Ca^{2+} concentrations. The black points are experimental data (individual measurements replotted from Kochubey and Schneggenburger (2011)). Solid lines represent the median release latencies and mean peak release rates predicted by the model from 1000 repetitions per simulated $[Ca^{2+}]_i$. The shaded areas indicate the 95% prediction interval of the model. The models with M_{slots}<3 failed to reproduce data, whereas models with M_{slots}≥3 agreed with data. Optimization and simulation were performed using a variable RRP size (Figure 2 – figure supplement 1). **B)** Minimum cost value as a function of M_{slots}. With M_{slots}=3 the minimum cost value was obtained, indicating the best correspondence to experimental release latencies and peak release rates. The point colors correspond to the color scale in panel G. **C)** Maximal slope of logarithm of simulated peak release rate vs logarithm of $[Ca^{2+}]_i$. For M_{slots}<3 the model failed to reproduce the Ca^{2+} dependency of release rates. **D-E)** The number of dual bindings at the time point of fusion for M_{slots}=3 (D) and M_{slots}=6 (E) determined from simulations of 10^4 SVs using three different $[Ca^{2+}]_i$. Most fusions took place after forming 3 or 4 dual bindings, even when allowing more dual bindings to form. A larger set of Ca^{2+} stimuli was also explored (Figure 2 – figure supplement 2 and Figure 2 - figure supplement 3). Forcing a model with M_{slots}=6 to fuse after 5/6 dual bindings were formed could not describe the experimental data and showed a too steep Ca^{2+} dependency of release (Figure 2 – figure supplement 4). **F)** The change in the energy barrier induced by dual binding formation (E_{syt}) as a function of M_{slots}. E_{syt} was computed from the fitted *f* values and was approximately constant for M_{slots}≥3. **G)** Exploring cost values in the parameter space for a model with M_{slots} =3. With *f* fixed at the best fit value (*f*=128), we determined the cost value of all combinations of 30 choices of the three free parameters, α, γ and [PI(4,5)P_2]. As the added delay

227 only leads to a vertical shift in the release latencies plot (see Figure 2 – figure supplement 5), this parameter was
228 optimized for each choice of the other free parameters to minimize the costs. The plot shows a subset of the
229 parameter combinations, and the colors indicate the cost value at each point. The color scale is linear below 1
230 and logarithmic above 1, and points with a cost value >1 are smaller for better visibility. The darkest blue colored
231 ball represents the overall minimum cost value in this parameter search and agrees with the best fit obtained.
232 The effect of varying each of the free parameters on release latencies and peak release rates can be seen in
233 Figure 2 – figure supplement 5. **H)** Minimum cost value as a function of *f* for a model with M_{slots} =3. For each
234 choice of *f* the model was fit to experimental data. This parameter exploration found the same minimum in the
235 parameter space as found by fitting all free parameters. Simulation scripts can be found in Source code 1. Results
236 depicted in Figure 2 and its figure supplements can be found in Figure 2 - source data 1.

237

238 The best fit parameters for three slots revealed rapid association rate constants for Ca^{2+} and $PI(4,5)P_2$
239 to the C2B domain and $PI(4,5)P_2$ levels corresponding to a concentration of ~1 µM in an in vitro setting
240 (Table 2). Predicted responses obtained using the best-fit parameters were sensitive to changes of
241 either of these parameters (Figure 2 – figure supplement 5). For instance, higher levels of $PI(4,5)P_2$
242 decreased the release latencies and increased the rate of fusion, and changing the Ca^{2+} association
243 rate constant (α) affected the release latencies much more than changing the $PI(4,5)P_2$ association rate
244 constant (γ). We verified that these parameters represent unique solutions by systematically exploring
245 the parameter space with *f* (which relates to the lowering of the fusion barrier for each syt dual-binding
246 $Ca^{2+}/PI(4,5)P_2$) fixed to the best fit value (*f*=128), which revealed a clear minimum at the best fit
247 parameters (Figure 2G, darkest ball). We furthermore confirmed that this *f* value was optimal by
248 systematically varying *f* and fitting all other parameters (Figure 2H).

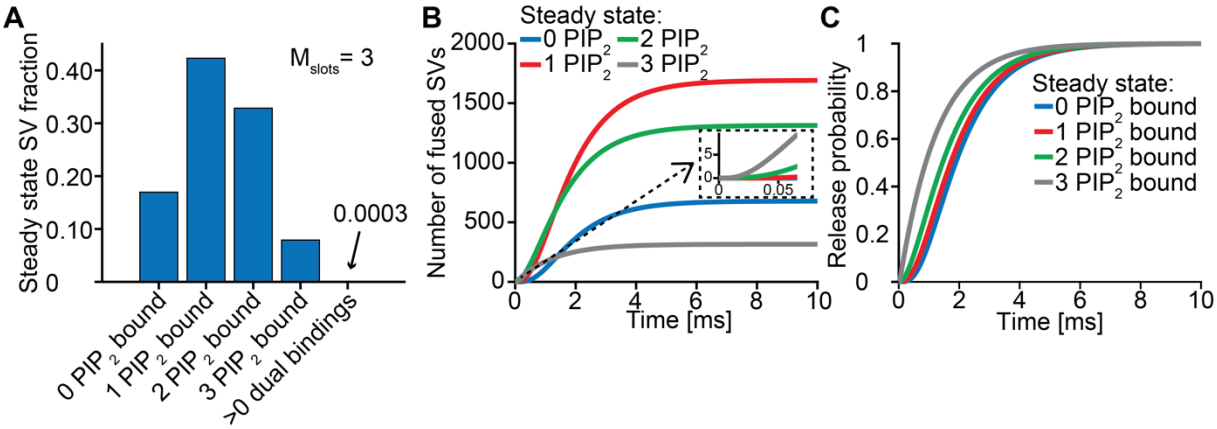

249
250 **Figure 3: Syts binding to $PI(4,5)P_2$ prior to Ca^{2+} stimulus underlies very fast SV fusion. A)** $PI(4,5)P_2$ binding status
251 of SVs at steady state. At resting $[Ca^{2+}]_i$ of 50 nM, more than 40 % of SVs have bound a single $PI(4,5)P_2$ molecule,
252 more than 30 % have bound two $PI(4,5)P_2$, while less than 10 % have bound three $PI(4,5)P_2$. Close to no SVs form
253 dual bindings at steady state. **B)** Cumulative fusion of SVs after 50 µM step Ca^{2+} at t=0, grouped according to their
254 initial $PI(4,5)P_2$ binding state. During the first ~0.5 ms, release is dominated by SVs having two or three syts bound
255 to $PI(4,5)P_2$ prior to the stimulus. The insert shows that the SVs having prebound three $PI(4,5)P_2$ constitute the
256 majority of the first five SVs that fuse in response to the Ca^{2+} step and therefore have largely impacted the release
257 latency. **C)** Cumulative release probability of SVs over time after 50 µM step Ca^{2+} at t=0, grouped according to
258 initial $PI(4,5)P_2$ binding state. The dominance of SVs having pre-bound to $PI(4,5)P_2$ with two or three syts in panel
259 B is explained by their high release probability compared to SVs with no or only one $PI(4,5)P_2$ bound. Figure 3 -
260 figure supplement 1 shows the same analysis for a model with M_{slots}= 6. Simulation scripts can be found in Source
261 code 1. Depicted simulation results can be found in Figure 3 - source data 1.

262 **The number of syt proteins pre-associated to PI(4,5)P_2 at rest influences the SV's Ca^{2+} responsiveness**

263 The steady state concentration of PI(4,5)P_2 determines the probability of syts associating to PI(4,5)P_2
264 at rest. With the best fit parameters, our model predicts that at rest ($[Ca^{2+}]_i$=50 nM) most SVs associate
265 to PI(4,5)P_2 by engaging one (~42%), two (~33%) or three (~8%) syts (Figure 3A, see Figure 3 – figure
266 supplement 1 for behavior in the model with M_{slots}=6). With a step-like Ca^{2+} stimulus to 50 µM, SVs with
267 two or three pre-associated syts mediated most of the fastest (<0.5 ms) SV fusions (Figure 3B).
268 Consequently, changing the steady state PI(4,5)P_2 concentration (which changes the number of pre-
269 associated syts/SVs) largely impacted the release latencies (defined as the timing of the fifth SV that
270 fuses (Kochubey and Schneggenburger, 2011) Figure 2 – figure supplement 5). Due to the allosteric
271 coupling, the Ca^{2+} affinities of syts prebound to PI(4,5)P_2 are increased and SVs with more PI(4,5)P_2
272 interactions are more responsive to the Ca^{2+} stimulus (Figure 3C). Thus, at the single SV level, the
273 number of pre-associated syts to PI(4,5)P_2 at rest plays a role in very fast (submillisecond) SV release
274 and causes heterogeneity in release probability among RRP SVs (Wolfel et al., 2007).

275

276 **Allosteric stabilization of Ca^{2+}/PI(4,5)P_2 dual binding is necessary to synchronize multiple C2B**
277 **domains for fast SV fusion**

278 An important feature of our model is the inclusion of a positive allosteric interaction between Ca^{2+} and
279 PI(4,5)P_2 binding to the C2B domain which we based on increased affinities measured *in vitro* (van den
280 Bogaart *et al.*, 2012). To explore the physiological relevance of this allostericity, we investigated how
281 individual SVs engaged their syt C2B domains in Ca^{2+}/PI(4,5)P_2 dual binding in response to a stepwise
282 increase of $[Ca^{2+}]_i$ to 50 µM (Figure 4A) with or without this allosteric coupling. We did this by following
283 the fate of four randomly chosen RRP SVs in stochastic simulations (Figure 4B). Under normal
284 conditions (with allostericity) syt C2B domains quickly associated both Ca^{2+} and PI(4,5)P_2 and their
285 respective allosteric stabilization slowed the dissociation of either species resulting in a lifetime of their
286 dual binding of ~1.3 ms on average. This enabled the successive engagement of three dual-bound C2B
287 domains at all four investigated SVs which induced their fusion within 4 ms (the average waiting time
288 for fusion with three dual-bound syts was ~1.1 ms)(Figure 4B, fusion indicated by circles). By inspecting
289 the average behavior of the entire RRP of SVs it became clear that the overall release rate closely
290 followed the population of SVs engaging three C2B domains in dual Ca^{2+}/PI(4,5)P_2 binding, illustrating
291 the importance of engaging three syts for fast SV fusion (Figure 4C). We also simulated the postsynaptic
292 response produced by this NT release by convolving the SV release rate with a typical postsynaptic
293 response to the fusion of a single SV (see Methods), which revealed synchronous and large Excitatory
294 Post Synaptic Currents (EPSCs)(Figure 4D).

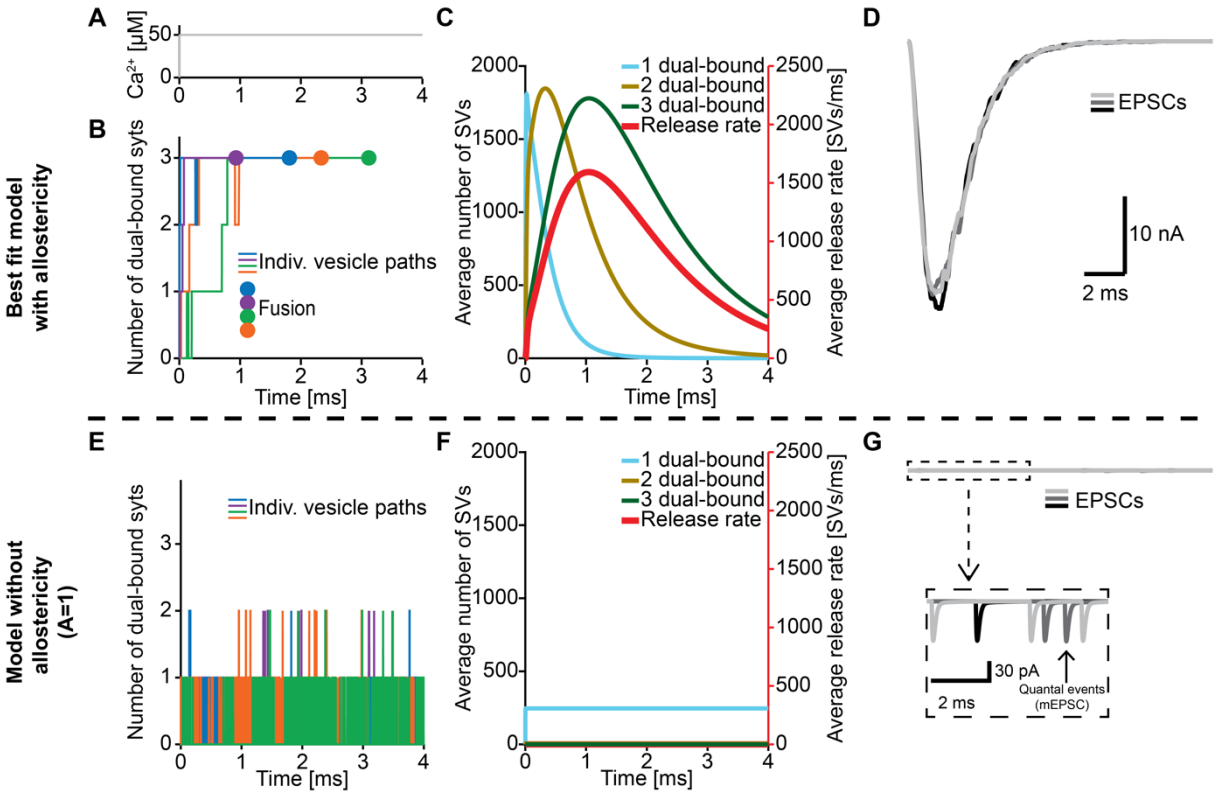

Figure 4: The positive allostericity between Ca^{2+} and $PI(4,5)P_2$ allows multiple syt C2B domains to engage in in $Ca^{2+}/PI(4,5)P_2$ dual binding. A) Ca^{2+} signal used in simulations ($[Ca^{2+}]_i$=50 µM). This constant Ca^{2+} concentration was used for all simulations depicted in this figure. **B)** The path towards fusion for four example SVs using stochastic simulations of the best fit model (with allostericity). The differently colored graphs show the number C2B domains engaging in $Ca^{2+}/PI(4,5)P_2$ dual binding for the four example SVs. The large dots indicate SV fusion. **C)** Average number of SVs having one (blue), two (olive) and three (green) C2B domains engaging in $Ca^{2+}/PI(4,5)P_2$ dual binding and the fusion rate (red) over time in simulations including the entire RRP. In the best fit model, the number of SVs with three syts dual-binding $Ca^{2+}/PI(4,5)P_2$ peaks approximately at the same time as the fusion rate. The decrease in number of SVs with one or two C2B domains dual binding $Ca^{2+}/PI(4,5)P_2$ reflects formation of additional dual bindings. The decrease in total number of SVs is caused by fusion of RRP vesicles. **D)** Excitatory Postsynaptic Currents (EPSCs) from three stochastic simulations with a fixed RRP size of 4000 SVs. The model predicts synchronous EPSCs with a small variation caused by the stochasticity of the molecular reactions. **E)** The path towards fusion for four example SVs (similar to panel A) in the model without allostericity in stochastic simulation. All parameters other than the allosteric factor (*A*) are the same as in the best fit model. Without stabilization, the syts quickly engage *and* disengage in $Ca^{2+}/PI(4,5)P_2$ dual binding and rarely more than one syt engages in dual binding. Formation and dissociation of Individual dual-bound syts is too fast to distinguish on the time scale depicted here. No fusions occurred in the depicted simulations. **F)** Average number of SVs having one (blue), two (olive) and three (green) syts engaging in $Ca^{2+}/PI(4,5)P_2$ dual binding and the fusion rate (red) over time in the model without allostericity. Almost no SVs form more than one syt dual binding $Ca^{2+}/PI(4,5)P_2$, which results in a very low fusion rate. **G)** EPSCs from three stochastic simulations and with a fixed RRP size of 4000 SVs. A model lacking allostericity only shows sporadic, individual release events. The insert shows a zoom-in of the first 6 ms of simulation and makes single SV fusion events giving rise to quantal, 'miniature' mEPSCs visible. Fitting the model without the allosteric effect to the experimental data was unsuccessful (Figure 4 – figure supplement 1). Simulation scripts can be found in Source code 1. Results from fitting the model without allosteric effect can be found in Figure 4 - source data 1.

323 We then explored what would happen without the allosteric stabilization of Ca^{2+}/PI(4,5)P_2 dual
324 binding (by setting A=1; Figure 4E). In this case, the C2B domains still quickly associated Ca^{2+} and
325 PI(4,5)P_2, but without the allosteric slowing of Ca^{2+}/PI(4,5)P_2 dissociation the lifetime of dual-bound
326 C2B domains was dramatically reduced (to an average of ~0.0003 ms). This made it very improbable
327 to engage multiple C2B domains in dual Ca^{2+}/PI(4,5)P_2 binding (Figure 4E). In turn, without the
328 simultaneous engagement of multiple syts dual-binding Ca^{2+}/PI(4,5)P_2, NT release became very
329 unlikely. In fact, none of the randomly chosen four RRP SVs fused within 4 ms (Figure 4E). Inspection
330 of the average behavior of the entire RRP revealed that only few SVs engaged more than one syt C2B
331 domain in dual Ca^{2+}/PI(4,5)P_2 binding, resulting in a very low fusion rate (Figure 4F). Correspondingly,
332 postsynaptic EPSCs were severely disrupted, and most release events were ill-synchronized single SV
333 fusion events (Figure 4G). It was furthermore not possible to fit a model without the allosteric
334 stabilization to the experimental dataset (Figure 4 – figure supplement 1). Thus, the positive allosteric
335 coupling between Ca^{2+} and PI(4,5)P_2 is fundamental for the syts to simultaneously and persistently
336 engage multiple C2B domains per SV in Ca^{2+}/PI(4,5)P_2 dual binding.

337

338 **Many syt per SV speed up exocytosis by increasing the probability of Ca^{2+}/PI(4,5)P_2 dual binding**
339 Our model strongly suggests that no more than three syts simultaneously binding Ca^{2+} and PI(4,5)P_2
340 are required to promote fast SV fusion (Figure 2). Yet, a total of 15 copies are expressed per SV on
341 average (Takamori *et al.*, 2006), which raises the question why SVs carry such excess and whether and
342 how the additional syt copies contribute to the characteristics of Ca^{2+}-induced synaptic transmission.
343 To investigate this, we simulated Ca^{2+} uncaging experiments with reduced numbers of syts per SV while
344 keeping all other parameters in the model constant. With fewer syts, release latencies increased and
345 peak release rates reduced. Defects were particularly prominent for reductions to less than three
346 copies per SV (Figure 5A). Further exploration indicated that this was because it took SVs longer to
347 simultaneously engage three C2B domains in dual Ca^{2+}/PI(4,5)P_2 binding and that fewer SVs reached
348 this state (Figure 5B).
349 While Ca^{2+} uncaging stimuli are exquisitely suited to map the full range of synaptic responses,
350 synaptic transmission is physiologically triggered by APs that induce short-lived Ca^{2+} transients. To
351 stochastically predict responses to such time-varying Ca^{2+} stimuli we implemented our model using a
352 Gillespie algorithm. After verifying that this model implementation agrees with the initial
353 implementation (Figure 5 – figure supplement 1), we simulated responses to a typical AP-induced Ca^{2+}
354 wave RRP SVs experience (Figure 5C, top panel). With 15 syts per SV, AP-induced EPSCs were large and
355 synchronous, but reducing their number decreased response amplitudes (Figure 5C). Removal of one
356 syt already reduced the average EPSC amplitude by ~10% and removal of half (7/15) of its copies

reduced it by ~72% (Figure 5 – figure supplement 2, for representative example traces see Figure 5C). Note, however, that our model only describes the functioning of syt1/ syt2 and therefore does not include other Ca^{2+}-sensors, like syt7 and Doc2B, which may mediate release in case of syt1/ syt2 loss (Bacaj *et al.*, 2013; Kochubey *et al.*, 2016; Kochubey and Schneggenburger, 2011; Luo and Sudhof, 2017; Sun *et al.*, 2007; Wen et al., 2010; Yao et al., 2011).

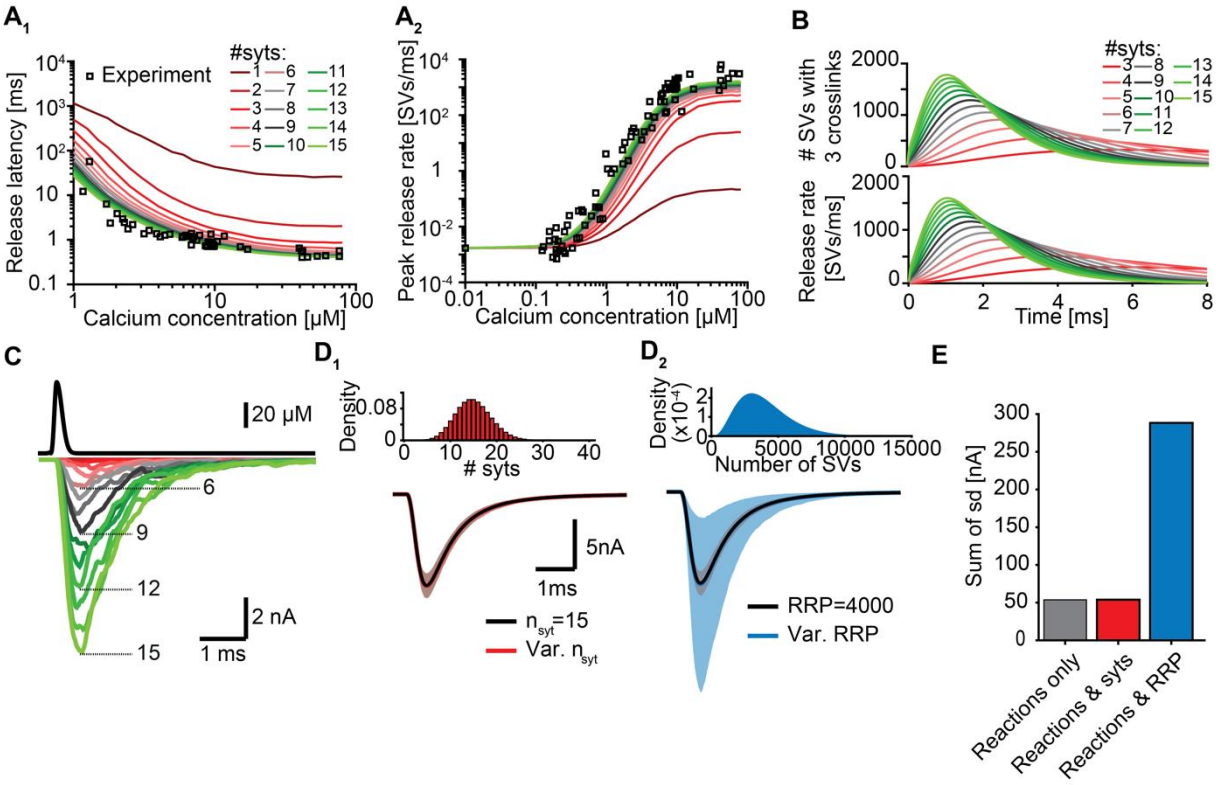

Figure 5: Simulations with reduced syt expression predict a reduction in SV fusion. A) Model predictions of median release latencies (A_1) and mean peak release rates (A_2) as a function of $[Ca^{2+}]_i$ for different numbers of syts per SV. All simulations were performed with 1000 repetitions using the best fit parameters obtained by fitting with n_{syts} = 15. Experimental data points are replotted from (Kochubey and Schneggenburger, 2011). **B)** The average number of SVs with three dual bindings formed (top) and release rate (bottom) as a function of time for 3-15 syt copies per SV from simulations with a Ca^{2+} flash of 50 µM. **C)** Predicted AP-evoked responses (bottom) simulated using a realistic Ca^{2+} transient (top) (Wang et al., 2008) for different numbers of syts per SV. The AP-evoked response shown at the bottom are representative single stochastic simulations with an amplitude closest to the mean amplitude of 200 repetitions. Increasing $[PI(4,5)P_2]$ for each choice of $n_{syt} \geq 3$ could fully rescue release latencies, release rates, and evoked responses (Figure 5 – figure supplement 2). **D)** Variability in simulated AP-evoked responses for a model with a variable number of syts and an RRP size of 4000 (D_1, red, bottom) and a model with a variable RRP size and 15 syts per SV (D_2, blue, bottom) compared to the variance induced by the stochasticity of the reactions only (with fixed number of SVs and syts, grey). Solid lines depict mean traces and the shaded area indicates the 95% prediction interval. Simulations with 1000 repetitions. Top panels show the probability density distributions of the number of syts (Poisson distribution, lambda =15) and of the number of SVs (gamma distribution, mean of 4000 SVs, standard deviation of 2000 SVs, outcome rounded to nearest integer). **E)** Quantification of the variance in the traces introduced by the stochasticity of the model reactions (grey), by the stochasticity of model reactions and variable syt number (red), and by the stochasticity of model reactions and variable RRP size (blue) by computing the sum of the standard deviation (sd) determined over the entire trace (0-6 ms, 300 data points). Simulation of the individual syts using the Gillespie algorithm agreed with simulations using the analytical solution of the Markov model (Figure 5 – figure supplement 1 and Methods). Simulation scripts can be found in Source code 1. Simulation results shown in this figure can be found in Figure 5 - source data 1.

386

387 As the number of syts per SV has a large impact on fusion kinetics we wondered to what extent
388 fluctuations in the number of syts per SV affected the variance in AP-evoked responses in case of their
389 imperfect sorting. Strikingly, however, varying the number of syts per SV over a large range (Poisson
390 distribution with mean = 15, Figure 5D$_1$,E, top panel) did not increase the variability of AP-evoked in
391 synaptic responses while fluctuations of the RRP size largely impacted them (Figure 5D$_2$,E). This shows
392 that although release kinetics strongly depend on the average number of syts per SV, the system is
393 rather insensitive to fluctuations around this number between individual SVs. Taken together, our data
394 show that although only a subset of syts are required to simultaneously bind Ca^{2+} and PI(4,5)P_2 to
395 induce fusion, all SV syts contribute to the high rates of NT release by increasing the probability that
396 several (i.e. three) syts simultaneously engage in dual Ca^{2+}/PI(4,5)P_2 binding.

397 Besides the number of syts, the PI(4,5)P_2 levels also determine how likely it is for syts to engage
398 in dual Ca^{2+}/PI(4,5)P_2 binding at an SV (see Figure 3 and Figure 2 – figure supplement 5). We therefore
399 reasoned that upregulation of PI(4,5)P_2 levels could potentially compensate for reduced syt
400 expression. To investigate this, we refitted the models with reduced syt levels to the experimental Ca^{2+}
401 uncaging data (Kochubey and Schneggenburger, 2011) and only allowed the PI(4,5)P_2 concentration in
402 the slots ([PI(4,5)P_2]) to vary. Strikingly, increasing [PI(4,5)P_2] fully rescued the characteristics of NT
403 release upon reductions in syt levels down to 3 syts per SV (corresponding to an 80% reduction) by
404 restoring number and speed of C2B domains engaging in Ca^{2+}/PI(4,5)P_2 dual binding (Figure 5 – figure
405 supplement 2A-C). The required increase in [PI(4,5)P_2] ranged from ~1.1x (14 syts) to ~10x (3 syts,
406 Figure 5 – figure supplement 2D). These elevations also fully restored simulated AP-evoked responses
407 when at least three syts per SV were present (Figure 5 – figure supplement 2E-F). Altogether, these
408 data indicate that upregulating [PI(4,5)P_2] is a potential, powerful compensatory mechanism to rescue
409 reductions of NT release in case the number of (functional) syts per SV is reduced to no less than three.
410 We note that this compensatory mechanism may complicate experimentally observed effects of
411 stoichiometric changes.

412

413 **Evaluation of mutants affecting Ca^{2+} binding to the C2B domain reveals diverse effects on AP-evoked**
414 **transmission**

415 Ca^{2+} sensing of syts depends on negatively charged aspartate (D) sidechains of the C2B domain whose
416 positions are optimal to bind Ca^{2+} ions (Fernandez *et al.*, 2001). The local negative charges of the Ca^{2+}
417 binding sites are reduced/neutralized upon Ca^{2+} binding. The Ca^{2+} binding pockets of the C2B domain
418 have been extensively studied using various mutations (Bradberry et al., 2020; Guan et al., 2017;
419 Kochubey and Schneggenburger, 2011; Lee *et al.*, 2013; Mackler *et al.*, 2002; Nishiki and Augustine,

420 2004; Shin et al., 2009). Mutations that remove or invert the negative charge of the Ca^{2+} binding sites
421 (by mutation to asparagine (N) or lysine (K), 'DN' or 'DK') block Ca^{2+} binding and severely reduce
422 exocytosis, even when co-expressed together with the wildtype protein (Bradberry *et al.*, 2020;
423 Kochubey and Schneggenburger, 2011; Lee *et al.*, 2013; Mackler *et al.*, 2002). Other mutations also
424 interfere with Ca^{2+} binding and exocytosis but hold the same pocket charge (e.g. mutation to
425 Glutamate, 'DE') (Bradberry *et al.*, 2020). While both types of mutations may similarly interfere with
426 Ca^{2+} binding, they may differentially affect the allosteric mechanism. The allosteric coupling between
427 the Ca^{2+} and PI(4,5)P_2 binding sites might be (in part) mediated by electrostatic interactions (van den
428 Bogaart *et al.*, 2012), which would imply that the negatively charged Ca^{2+} binding pocket repels
429 PI(4,5)P_2 until Ca^{2+} reverses the electrostatic charge, and vice versa. Following this assumption, charge
430 altering mutations within the Ca^{2+} binding pockets ('DN', 'DK') would partially activate the allosteric
431 coupling mechanism and thereby affect the domain's PI(4,5)P_2 affinity (which would not be the case in
432 mutants conserving the charges ('DE')). We explored this in our model using two different hypothetical
433 Ca^{2+} site mutants (i.e. mutations that do or do not affect PI(4,5)P_2 affinity; Figure 6A). We investigated
434 the effect of these mutants on AP-induced synaptic transmission under homozygous and heterozygous
435 expression conditions (combined expression of mutant and WT with a total of 15 syts per SV; Figure
436 6B).

437 The first mutant, the "*Ca^{2+}-binding*" mutant, had a lower Ca^{2+} affinity (10x$K_{D,2Ca2+}$), but all other
438 properties were the same as in the WT C2B domain. This mutant might be equivalent to mutation of
439 the binding pocket which conserves its charge (e.g. 'DE'). When homozygously expressed, this mutant
440 showed eEPSCs with a ~50% reduced amplitude and faster kinetics compared to the WT condition
441 (Figure 6C_1, Figure 6D top). Heterozygous expression (8 WT and 7 mutant syts per SV) only caused a
442 small decrease in mean eEPSC amplitude compared to the expression of 15 WT syts per SV (Figure 6C_1-
443 D, bottom), showing that this mutant is relatively mild.

444 The second hypothetical mutation was designed to not only abolish Ca^{2+} binding, but to also
445 mimic the Ca^{2+}-bound state. Thereby this mutant featured a high PI(4,5)P_2 affinity as if the allosteric
446 interaction between Ca^{2+} and PI(4,5)P_2 was permanently 'on'. This might represent an extreme
447 example of a mutation electrostatically reducing/inverting the negative charges of the Ca^{2+} binding
448 pocket (e.g. 'DN', 'DK'). We termed this mutant the "*no Ca^{2+} binding, A-on*" mutant (Figure 6A). This
449 mutant showed no NT release in response to the Ca^{2+} transient in a homozygous condition (Figure 6C_2-
450 D, top), which is explained by its inability to bind Ca^{2+}. A major detrimental effect of the mutant was
451 observed when co-expressed with the wildtype protein: When half of the syts on the SV were mutated
452 (heterozygote), the amplitude of simulated eEPSCs was strongly reduced (Figure 6C_2-D, bottom).
453 Merely four mutant proteins expressed together with 11 WT proteins already decreased eEPSC
454 amplitudes by ~70% (Figure 6D, bottom), indicating a strong dominant negative effect. The strong

455 inhibition is a result of the mutant's increased PI(4,5)P_2 affinity leading to occupation of PI(4,5)P_2
456 binding slots on the membrane with this Ca^{2+}-insensitive mutant which blocks the association of the
457 Ca^{2+} sensitive- and SV fusion promoting WT proteins. In comparison, a mutant not able to bind Ca^{2+}
458 but having a normal PI(4,5)P_2 affinity (*"no Ca^{2+} binding, A-off"* mutant, which could represent a more
459 extreme form of the 'DE' mutant) had a much weaker effect (Figure 6 - figure supplement 1). This
460 indicates that the allosteric interaction between Ca^{2+} and PI(4,5)P_2 can play a prominent role in the
461 severity of mutations.
462

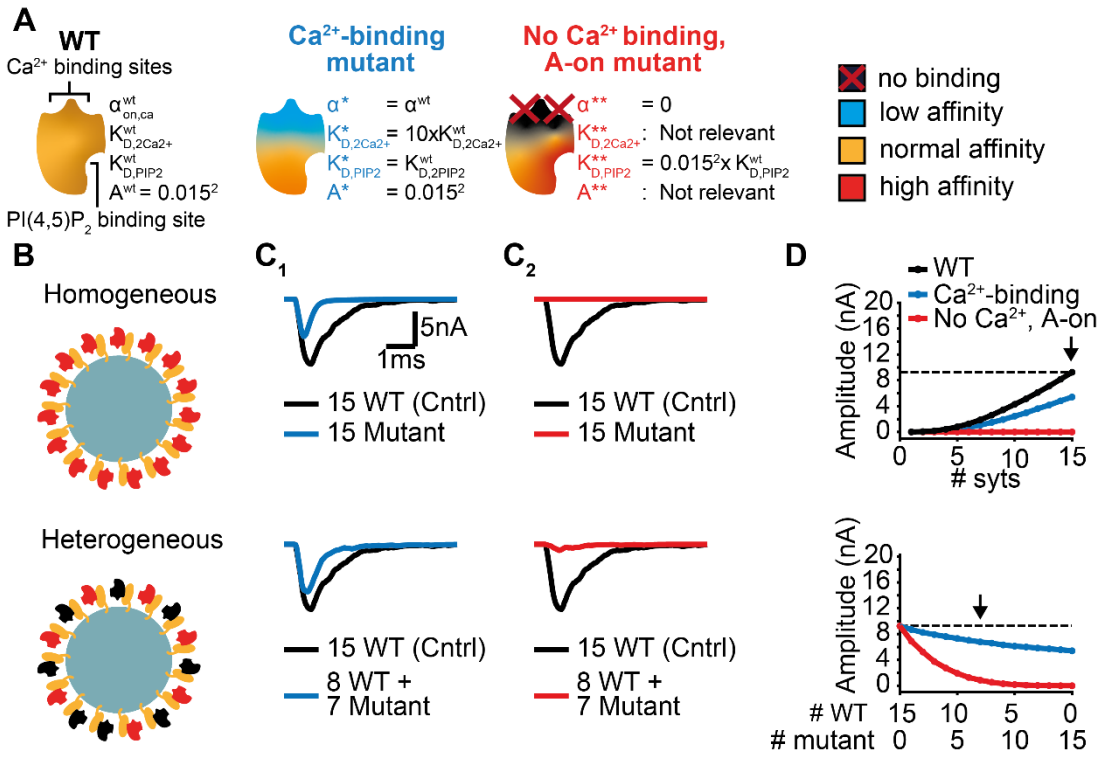

463

464 **Figure 6: Systematic evaluation of the effect of mutant syts on simulated AP-evoked fusion. A)** Illustration of a
465 WT syt and two mutant syts. The *"Ca^{2+}-binding"* mutant has a lower affinity for Ca^{2+} ($K_{D,2Ca2+}$ 10x increased, i.e. β
466 10x increased). The *"no-Ca^{2+} binding, A-on"* mutant is not able to bind Ca^{2+} and has a high binding affinity for
467 PI(4,5)P_2, which is equal to the affinity for PI(4,5)P_2 when the allostericity between Ca^{2+} and PI(4,5)P_2 is "active"
468 in WT syts (Ca^{2+}-bound state). Because of the inability to bind Ca^{2+}, allosteric interactions between Ca^{2+} and
469 PI(4,5)P_2 are not possible in this mutant. **B)** Illustration of homogeneous (top) and heterogeneous expression
470 (bottom) of the mutants. Mutant syts are depicted in red, WT syts are depicted in black. **C)** Representative,
471 stochastically simulated AP-evoked responses with homozygous (top, 15 mutant syt copies) and heterozygous
472 (bottom, 8 WT and 7 mutant syt copies) expression of the different mutants (C_1: *"Ca^{2+}-binding"* mutant, in blue;
473 C_2: *"no Ca^{2+} binding, A-on"* mutant, in red). For each of the settings a representative trace of a condition with 15
474 WT syts is shown in black (control condition). A third mutation, the *"no Ca^{2+} binding, A-off"* was also explored
475 (Figure 6 – figure supplement 1). **D)** Mean amplitudes of simulated AP-evoked responses (n=200) for the
476 homogeneous (top), heterogeneous (bottom) of the different mutants, and WT syt (for homozygous condition
477 only). Dotted line indicates the mean amplitude of simulated eEPSCs with 15 copies of WT syt (control). Arrow
478 indicates the condition that is depicted in panels C. Simulation scripts can be found in Source code 1. Results
479 from simulations can be found in Figure 6 - source data 1.

480

481 **Rapid changes of accessible PI(4,5)P_2 dramatically impact synaptic short-term plasticity**

482 In our model we describe the PI(4,5)P_2 levels in concentration units, because our model is based on syt
483 affinities for Ca^{2+} and PI(4,5)P_2 determined *in vitro* (van den Bogaart *et al.*, 2012). The estimated
484 concentration of PI(4,5)P_2 not only depends on the local density of PI(4,5)P_2 in the membrane, but also
485 on the accessibility syt has to PI(4,5)P_2. While all species (Ca^{2+}, PI(4,5)P_2, and syt C2B) are
486 homogenously accessible in the aqueous solution of the *in vitro* setting (van den Bogaart *et al.*, 2012),
487 at the synapse the syt C2 domains have constrained motility due to their vesicular association and
488 PI(4,5)P_2 is restricted to (clusters on) the plasma membrane (Milosevic et al., 2005; van den Bogaart *et*
489 *al.*, 2011a). This implies that the positioning of SVs with respect to the plasma membrane has an impact
490 on the PI(4,5)P_2 concentration accessible to syts. We so far assumed that all syts of RRP SVs are exposed
491 to the same PI(4,5)P_2 levels (which could be the case if all vesicles are similarly docked to the plasma
492 membrane). However, when considering more complex stimulation paradigms such as repetitive AP
493 stimulation, this may no longer be valid as several studies reported activity-dependent changes in SV
494 positioning on a millisecond timescale (Chang *et al.*, 2018; Kusick et al., 2020; Miki et al., 2016). Such
495 changes may thus contribute to short-term plasticity, the alteration of responses on a millisecond
496 timescale (Abbott and Regehr, 2004; Kobbersmed et al., 2020; Neher and Brose, 2018; Silva et al.,
497 2021). Recent studies reported that mutations of positively charged amino acids of the C2B domain
498 (lysines, 'Ks', implicated in binding of PI(4,5)P_2 and/or the SNAREs and arginines, 'Rs' implicated in
499 binding the plasma membrane and/or the SNAREs resulted in a loss of SV docking and severely
500 reduced neurotransmission (Chang *et al.*, 2018; Chen *et al.*, 2021; Li *et al.*, 2006; Xue *et al.*, 2008).
501 Strikingly, SV docking in these mutants was rapidly restored within milliseconds after an AP which also
502 led to enhanced synaptic transmission in response to a second AP given 10 ms after the first (Chang *et*
503 *al.*, 2018). We explored such a situation in the context of our model by driving exocytosis with two
504 successive AP-induced Ca^{2+} transients and assuming either constant PI(4,5)P_2 levels for syts in wildtype
505 synapses (i.e. all RRP SVs similarly docked) or initially reduced and activity-dependent increasing
506 PI(4,5)P_2 levels for syts in mutant synapses (where SVs docked after the first AP) (Figure 7A). We
507 studied the consequence of a mutation that would only affect SV docking at steady state (as may be
508 the case upon mutation of the arginines 398 and 399 of mouse syt 1, 'R398,399Q') in (Figure 7). This
509 resulted in a markedly decreased initial response (Figure 7B,C), but repeated activation induced a large
510 facilitation of responses (indicated by a large paired pulse ratio: quotient of the second EPSC
511 amplitudes divided by the first) (Figure 7D). Mutations of the C2B domain that reduce its PI(4,5)P_2
512 affinity (as is likely the case upon mutation of the lysine residues 325 and 327 in syt1 or 327, 328 and
513 332 in syt2) may be more detrimental because even when the effective PI(4,5)P_2 concentration
514 accessible to syts is restored upon activity-dependent SV redocking, syt association to PI(4,5)P_2 will still

515 be less probable. We conclude that dynamic changes in the PI(4,5)P_2 levels accessible to syts - which
516 may be caused by activity dependent SV relocation – strongly impact synaptic short-term plasticity.

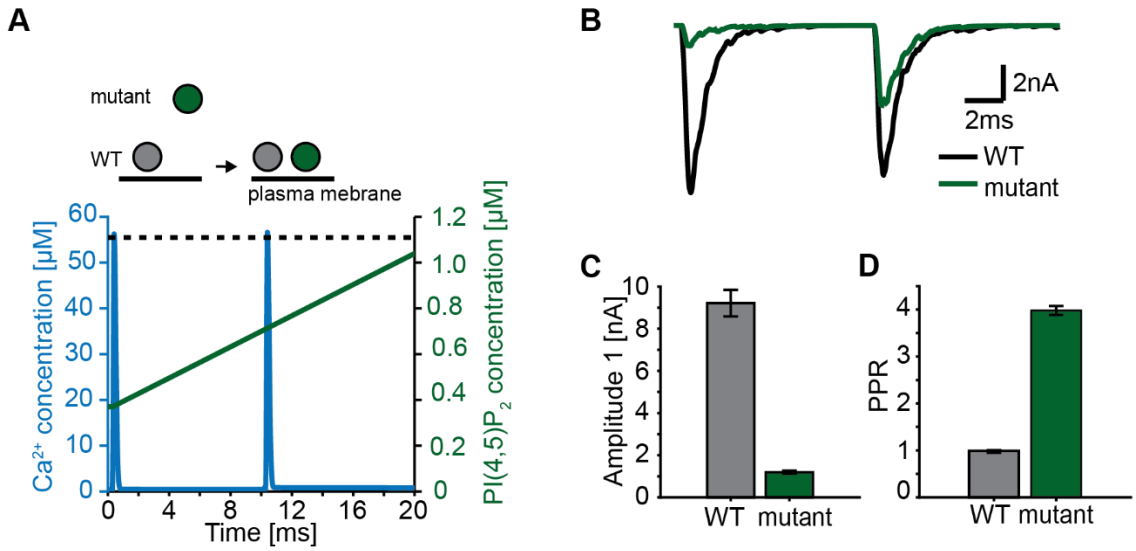

517

518 **Figure 7. Paired-pulse stimulation in a membrane binding syt mutant. A)** Time-course of $[Ca^{2+}]_i$ (blue) and
519 [PI(4,5)P_2](dashed black line: wildtype (WT), green line: mutant). Top panel illustrates the placement of vesicles
520 with respect to the PM for SVs expressing WT syt (grey SVs) and SVs expressing a syt mutant deficient in
521 membrane binding (green SVs, homozygous expression) before the first (left side of arrow) and second AP (right
522 side of arrow). In WT conditions, most SVs reside close to the PM before the onset of the first stimulus. Before
523 onset of the second pulse, WT SVs keep the same average distance to the PM. Mutant SVs, however, show a
524 large distance to the PM at the onset of the first stimulus. Before the onset of the second AP, mutant vesicles
525 move closer to the PM due to a Ca^{2+}-dependent mechanism (Chang *et al.*, 2018). The bottom panel shows the
526 Ca^{2+} (blue) and PI(4,5)P_2 (green) transients over time in a paired pulse stimulus (10 ms between stimuli). Due to
527 the increased distance between the SV and the PM in the membrane-binding mutant, mutant vesicles are
528 assumed to experience a lower [PI(4,5)P_2] (solid green line) compared to WT SVs (dotted, black line) at the start
529 of the first stimulus. Before the start of the second stimulus, mutant SVs move closer to the PM which increases
530 the experienced [PI(4,5)P_2] of these SVs. **B)** Representative eEPSCs simulated using the Ca^{2+}- and PI(4,5)P_2
531 transients depicted in A. **C)** Amplitude of the first eEPSC for WT and mutant. **D)** Paired-Pulse ratio (PPR) for WT
532 and mutant. Data in C and D show mean ± SEM, using 50 repetitions and a variable RRP size (see Methods for
533 details, the same RRP values were used for both the mutant and the WT condition). Simulation scripts can be
534 found in Source code 1. Depicted simulation results can be found in Figure 7 - source data 1.

535 ## Discussion

536 We here propose a quantitative, experiment-based model describing the function of syt in SV fusion
537 on a molecular level based on biochemical properties determined *in vitro*. In our model, syt acts by
538 lowering the energy barrier for SV fusion by dual binding to Ca^{2+} and PI(4,5)P_2. When allowing at least
539 three dual-bound syts per SV at a time, this model can explain the steep Ca^{2+} dependence of NT release
540 observed at the calyx of Held synapse (Kochubey and Schneggenburger, 2011). Exploring this model
541 led to the following conclusions:

542 1) The positive allosteric interaction between Ca^{2+} and PI(4,5)P_2 is crucial for fast SV fusion as it
543 stabilizes the dual-bound state which allows multiple syts to successively lower the energy
544 barrier for SV fusion;
545 2) At least three syts must simultaneously engage in Ca^{2+}/PI(4,5)P_2 dual binding for fast SV fusion
546 to achieve the speed and Ca^{2+} sensitivity inherent to synaptic transmission;
547 3) A high copy number of syts per SV ensures fast NT release by increasing the probability that
548 three syts engage in Ca^{2+}/PI(4,5)P_2 dual binding;
549 4) Binding of syts to PI(4,5)P_2 prior to the Ca^{2+} stimulus allows some SVs to fuse very fast
550 (submillisecond).
551 5) The molecular resolution of this model can be used to study consequences of mutations.
552

553 **A syt-dependent switch on the energy barrier for SV fusion**

554 Exocytosis is a highly energy-demanding reaction, for which the formation of the neuronal SNARE
555 complex provides the energy (Jahn and Fasshauer, 2012). In our model we assume that syts regulate
556 this process by lowering the activation energy barrier for exocytosis when they engage in Ca^{2+}/PI(4,5)P_2
557 dual binding. However, how Ca^{2+}/PI(4,5)P_2 dual binding to syt exactly reduces this energy barrier is not
558 known. One possibility is that the energy is provided by the SNAREs themselves and that Ca^{2+}/PI(4,5)P_2
559 dual binding to syt relieves a clamping function, which syt itself or the auxiliary protein complexin
560 exerts on the SNAREs (Courtney et al., 2019; Schupp *et al.*, 2016; Tang *et al.*, 2006; Zhou *et al.*, 2015;
561 Zhou *et al.*, 2017). Alternatively – or additionally – syt's dual binding Ca^{2+}/PI(4,5)P_2 might promote
562 SNARE-mediated fusion by changing the local electrostatic environment (Ruiter *et al.*, 2019; Shao et
563 al., 1997). Furthermore, dual-binding syts could bring SVs closer to the plasma membrane, potentially
564 below an upper limit for full SNARE complex assembly (Araç *et al.*, 2006; Chang *et al.*, 2018; Honigmann
565 *et al.*, 2013; Hui et al., 2011; Lin et al., 2014; Nyenhuis et al., 2019; van den Bogaart *et al.*, 2011b; Xue
566 *et al.*, 2008). In line with these hypothetical working mechanisms, our estimated effect each dual-
567 bound C2B domain has on the energy barrier height (4.85 k_bT) is similar to the estimated energy barrier

568 height for the final zippering step of the SNARE complex (Li et al., 2016). Syt's Ca^{2+}/PI(4,5)P_2 dual
569 binding might also promote fusion by inducing membrane curvature or favoring lipid rearrangement
570 (Lai et al., 2011; Martens *et al.*, 2007). In line with this reasoning, our estimated contribution of a syt
571 engaging in Ca^{2+}/PI(4,5)P_2 dual binding is similar to estimates of syt1 membrane binding energies
572 (Gruget *et al.*, 2020; Gruget et al., 2018; Ma et al., 2017). In our model, we assume that multiple syts
573 can simultaneously reduce the energy barrier for fusion. We here assumed that all syts exert the same
574 effect on this energy barrier for fusion and that the effects of more dual-bound syts are additive.
575 Whether or not this is the case will depend on the precise mechanism by which they shape the energy
576 landscape. We show here that the simplest model (constant and independent contribution) is
577 sufficient to reproduce the biological response.

578 Both the C2A and C2B domain of syt cooperate in SV exocytosis (Bowers and Reist, 2020;
579 Gruget *et al.*, 2020; Lee *et al.*, 2013; Wu *et al.*, 2021b). However, the exact role of the C2A domain in
580 triggering SV fusion remains debated (Fernández-Chacón *et al.*, 2002; Lee *et al.*, 2013; Paddock et al.,
581 2011; Sørensen et al., 2003; Stevens and Sullivan, 2003; Striegel et al., 2012). As mutation of the Ca^{2+}
582 binding pockets of the C2A domain did not affect the affinities of Ca^{2+} and PI(4,5)P_2 *in vitro* (van den
583 Bogaart *et al.*, 2012), we focused on the C2B domain in our model. This, however, does not imply that
584 our C2B-domain-based model, which fully recapitulates the physiological responses of the synapse,
585 does not indirectly describe properties of the C2A domain For instance, Ca^{2+} binding to the C2A domain
586 may influence the Ca^{2+} affinity for the C2B domain (Sørensen *et al.*, 2003),and this property may be
587 collapsed into other parameters of model (e.g. our estimate of the PI(4,5)P_2 concentration) that
588 similarly determine this.

589

590 **Allostericity buys time to synchronize syts**

591 Our modeling study proposes that the allostericity between Ca^{2+} and PI(4,5)P_2 binding is essential for
592 the syts to achieve fast, synchronous and sensitive NT release (van den Bogaart *et al.*, 2012) (Figure 4
593 – figure supplement 1). With their experiment, Van den Bogaart and colleagues (2012) determined
594 steady state affinities, which do not provide information on the association/dissociation rates. This
595 means that the allosteric effect may either be due to speeding up the association or slowing down the
596 dissociation of Ca^{2+}/PI(4,5)P_2 (Figure 1A). We here implemented the latter, a reduction of the
597 unbinding rates of both Ca^{2+} and PI(4,5)P_2 when both species were bound to the C2B domain, which
598 leads to a stabilization of the dual-bound state. A stabilization of the Ca^{2+}-bound state, which increases
599 the lifetime of the state, was also essential to reproduce the Ca^{2+} dependence of release in the
600 previously proposed five-site binding model (Heidelberger *et al.*, 1994; Schneggenburger and Neher,

601 2000). We here show in the context of our model that increasing the lifetime of Ca^{2+}/PI(4,5)P_2 dual
602 binding is particularly important to achieve fast fusion rates as it allows several C2B domains to
603 simultaneously engage to lower the fusion barrier (Figure 4). The drawback of the strong allosteric
604 interaction between the Ca^{2+} and PI(4,5)P_2 bindings sites might be its potential involvement in the
605 strong dominant-negative effects of some C2B domain mutations (Figure 6).
606

607 **The stoichiometry of the SV fusion machinery**

608 Each SV contains multiple syt copies (Takamori *et al.*, 2006), which can jointly participate in the fusion
609 process. However, the number of syts that can simultaneously engage with PI(4,5)P_2 located at the
610 plasma membrane, and thus can cooperate during fusion, is likely limited. There are several possible
611 explanations for this limit. First, the space between the vesicular and plasma membrane is limited and
612 crowded by many synaptic proteins (Wilhelm et al., 2014). In addition, plasma membrane association
613 of syt may require interaction with the SNAREs (de Wit *et al.*, 2009; Mohrmann *et al.*, 2013; Rickman
614 and Davletov, 2003; Zhou *et al.*, 2015), which limits the number of association points. Moreover, the
615 inhomogeneous distribution of PI(4,5)P_2 in the plasma membrane might put further constraints on
616 association of syt to PI(4,5)P_2 (Milosevic *et al.*, 2005; van den Bogaart *et al.*, 2011a). We found that at
617 least three PI(4,5)P_2 association sites ('slots') were required to explain the steep Ca^{2+} dependency of
618 neurotransmitter release (Figure 2 A-C). These findings are compatible with a cryo-EM analysis that
619 identified six protein complexes between docked SVs and plasma membrane (Radhakrishnan et al.,
620 2021). Interestingly, irrespective of the number of slots, for models with three or more slots our
621 analysis suggests that most fusion events at $[Ca^{2+}]_i$ > 1 μM occurred after engaging three syts in
622 Ca^{2+}/PI(4,5)P_2 dual binding (Figure 2 D-E). At lower $[Ca^{2+}]_i$ (0.5-1 μM, Figure 2 - figure supplement 2B
623 and Figure 2 – figure supplement 3B), the number of dual bindings leading to fusion was reduced to 1-
624 2, indicating that higher $[Ca^{2+}]_i$ recruits additional syts to increase fusion rates.

625 The predicted number of three syts involved in fast exocytosis matches experimental estimates
626 of the number of SNARE-complexes zippering for fast vesicle fusion (Arancillo et al., 2013; Mohrmann
627 et al., 2010; Shi et al., 2012; Sinha et al., 2011) (but higher estimates in the number of SNARE complexes
628 actively involved in fusion have also been reported (Wu et al., 2017)). Moreover, our model is
629 consistent with a previous model of neurotransmitter release at the frog neuromuscular junctions that
630 estimated that fusion is triggered by the binding of two Ca^{2+} ions to each of three syts. That model,
631 which describes Ca^{2+} dynamics in the AZ in great detail, showed that many additional Ca^{2+} binding sites
632 (20-40) were required to enhance fusion probability, because the probability of having a single Ca^{2+}
633 molecule in the vicinity of SVs is extremely low (Dittrich et al., 2013). Similarly, in our model additional
634 syts promote SV fusion by increasing the collision probability of syts with Ca^{2+} and PI(4,5)P_2, and

635 thereby increase the probability of (multiple) syts engaging in Ca^{2+}/PI(4,5)P_2 dual-binding for fast
636 synaptic transmission (Figure 5). High protein abundance might also promote other collision-limited
637 processes in fusion of SVs, and may provide an intuitive explanation for the high abundance of
638 synaptobrevins on SVs (~70 copies) which may need to assemble into SNARE complexes downstream
639 of syt action (Takamori *et al.*, 2006; van den Bogaart *et al.*, 2011b).
640 Our model predicts that most RRP SVs have prebound PI(4,5)P_2 via one syt at rest (Figure 3A),
641 but it is the Ca^{2+}-induced, allosteric PI(4,5)P_2 affinity-increase that induces the dynamic assembly of
642 three C2B domains in Ca^{2+}/PI(4,5)P_2 dual binding. This is fundamentally different from studies
643 suggesting that 12-20 syts need to preassemble in higher-order complexes (rings) to execute their
644 function in fusion (Rothman et al., 2017). A testable property to distinguish these possibilities is the
645 sensitivity to reducing the number of syts per SV. If transmitter release relied on preassembled syt-
646 rings, it would immediately break down if the number of syts was reduced to one preventing ring
647 assembly, whereas our model predicts gradual effects (even for titration below n_{syt} =3) (Figure 5).
648
649 **Heterogeneity in PI(4,5)P_2 concentration between different RRP SVs**
650 The interaction between syt and PI(4,5)P_2 has been shown to be essential in SV exocytosis (Bai *et al.*,
651 2004; Li *et al.*, 2006; Wu *et al.*, 2021a), but also has been found to play a role in SV docking (Chang *et*
652 *al.*, 2018; Chen *et al.*, 2021). Consistently, we observed that at resting synapses the majority of SVs
653 (~83%) contain at least one syt bound to PI(4,5)P_2 in our model (Figure 3). The number of syts bound
654 to PI(4,5)P_2 per SV at rest highly influenced the release probability, leading to heterogeneity within the
655 RRP (Figure 3) (Wolfel *et al.*, 2007). As PI(4,5)P_2 levels have a large impact on release kinetics (Figure 2
656 – figure supplement 5, Figure 5 – figure supplement 2), heterogeneity between RRP vesicles might
657 further be enhanced by unequal PI(4,5)P_2 levels.
658 In our model, we described PI(4,5)P_2 levels in concentration units to constrain our model by
659 using in vitro PI(4,5)P_2 affinity measurements (van den Bogaart *et al.*, 2012). However, this
660 concentration does not only encompass the density of PI(4,5)P_2 in the plasma membrane, but also
661 includes the accessibility of syt to PI(4,5)P_2. Several studies have shown that PI(4,5)P_2 is distributed
662 heterogeneously over the plasma membrane, in clusters that contain a high PI(4,5)P_2 density
663 (Honigmann *et al.*, 2013; Milosevic *et al.*, 2005; van den Bogaart *et al.*, 2011a). Moreover, syts located
664 closer to the plasma membrane will have increased access to PI(4,5)P_2 ("see a higher PI(4,5)P_2
665 concentration") compared to those located further away. Taken together, this indicates that the
666 PI(4,5)P_2 concentration is likely to vary between RRP SVs and also between individual syts on the SV.
667 Furthermore, this implies that once a syt has engaged in PI(4,5)P_2 binding the successive engagement
668 of additional syts might be favored for some (those facing towards the PM) and disfavored for others
669 (those facing from the PM). While knowledge of these details could be helpful to construct a more

670 realistic version of our molecular model, we currently do not possess the methodology to measure
671 these properties. We therefore in our model simulated the simplest scenario where all syts have an
672 equal probability of engaging in PI(4,5)P_2 binding.

673 As the localization of syts with respect to the PM influences the accessibility of syt to PI(4,5)P_2,
674 mutations in synaptic proteins and stimulation protocols that alter SV docking will affect the PI(4,5)P_2
675 concentration as it is implemented in our model (Chang *et al.*, 2018; Chen *et al.*, 2021; Kusick *et al.*,
676 2020). Using a time-dependent PI(4,5)P_2 concentration, we here illustrated the impact this might have
677 on the short term plasticity of synaptic responses (Figure 7). This is a simplification, as we did not take
678 the individual SV/syt distances to the plasma membrane into account. This distance is affected by
679 several synaptic proteins, including syt1, Munc13 and Syt7 (Chen *et al.*, 2021; Imig et al., 2014; Liu et
680 al., 2016; Quade et al., 2019; Tawfik et al., 2021; Voleti et al., 2017). A role of these proteins in short
681 term plasticity is firmly established, yet precise mechanistic details are still lacking (Jackman et al.,
682 2016; Rosenmund et al., 2002; Shin et al., 2010). The extension of models based on molecular
683 interactions such as presented here should allow for the recapitulation of more complex synaptic
684 activity patterns relevant for neural processing. Particularly the molecular resolution of such models
685 will be useful to conceptualize the importance of specific molecular interactions for physiological and
686 pathological processes at the synapse.

687 ## Materials and Methods

688 In this paper we propose a model for SV fusion induced by Ca^{2+} and PI(4,5)P_2 binding to n_{syts} syts per
689 SV, with at most M_{slots} syts per SV engaging in PI(4,5)P_2 binding at the same time. We implemented the
690 model in two ways for different simulation purposes: (1) an implementation based on the analytical
691 solution of the model, and (2) an implementation following the Gillespie algorithm (Gillespie, 2007)
692 (Matlab procedures for simulations can be found in Source code 1). In the first implementation we
693 assume a constant $[Ca^{2+}]_i$, (allowing us to simulate Ca^{2+} uncaging experiments: SV reactions at a Ca^{2+}
694 level reached by the uncaging stimulus from a steady state starting point calculated for the resting Ca^{2+}
695 concentration of 50 nM), whereas the second version was implemented to allow for $[Ca^{2+}]_i$ to vary over
696 time (allowing us to simulate AP-evoked responses). Another important difference between the two
697 approaches is that the analytical solution describes the binding state of an entire SV and the Gillespie
698 version describes the binding state of each individual syt. Both implementations allow for stochastic
699 evaluation of the model. The first implementation is used in Figure 2, 2 supplement 4, 2 supplement
700 5, 3, 3 supplement 1, 4C-D,F-G, 4 supplement 1, 5A-B, 5 supplement 1A-B. The second implementation
701 is used to simulate the AP-evoked responses and individual SV binding states in Figures 2 supplement
702 2, 2 supplement 3, 4B,E, 5C-E, 5 supplement 1E-F, 6C-D, and 6 supplement 1, and 7B-D. Consistency
703 between the two approaches was validated by comparison of simulation result distributions in
704 quantile-quantile (Q-Q) plots (Figure 5 – figure supplement 2).

705

706 **SV states and possible reactions in the analytical version of the model**

707 In the analytical solution of the model, we describe for each SV the number of syts having bound two
708 Ca^{2+} ions, PI(4,5)P_2, or both species. Since syts were assumed to work independently, their order is not
709 relevant, and we therefore do not need to describe the binding state of each individual syt. The
710 possible binding states of an SV are described in Figure 1 – figure supplement 2. Each state is
711 represented by the triplet *(n,m,k)*, with *k* denoting the number syts having bound PI(4,5)P_2, *m* denoting
712 the number of syts having bound two Ca^{2+} ions, and *n* denoting the number of syts having bound both
713 species and thereby having formed a dual binding. n_{syts} is the total number of syts per SV. M_{slots} restricts
714 the number of syts having bound PI(4,5)P_2 simultaneously (this includes syts having bound PI(4,5)P_2
715 only (*k*), and those having formed a dual binding (*n*). Taken together, this implies that for all states in
716 the model, it holds that

717 $$k + m + n \leq n_{syts} \text{ and } k + n \leq M_{slots}$$

We numbered the states systematically following a lexicographic ordering, excluding the states that violate the inequalities described above. To illustrate, we write the ordering of all the states *(m,n,k)* with $n_{syts}=3$ and $M_{slots}=2$:

(0,0,0),(0,0,1),(0,0,2),(0,1,0),(0,1,1),(0,1,2),(0,2,0),(0,2,1),(0,3,0),(1,0,0),(1,0,1),(1,1,0),(1,1,1),(1,2,0),(2,0,0),(2,1,0).

Besides these binding states, an additional state, *F*, describes whether the SV has fused. With $n_{syts}=15$ and $M_{slots}=3$, a single SV in our model has 140 + 1 states. From any state, there are at most 9 possible reactions, one being SV fusion and the other 8 being (un)binding of Ca^{2+} or $PI(4,5)P_2$ to/from a syt. The rates for the possible reactions of a single SV in this model are summarized in Table 3. In many cases, only a subset of the 8 (un)binding reactions are allowed because of the inequalities above (noted under "Condition" in the table).

The reaction rates of (un)binding Ca^{2+} or $PI(4,5)P_2$ are calculated as the number of syts available for (un)binding (computed using n_{syts}, *n, m, k)* times the reaction rate constant (α, β, γ, δ), and, in the case of binding reactions, times the concentration of the ligand ($[PI(4,5)P_2]$ or $[Ca^{2+}]$). We assumed binding of two Ca^{2+} ions to a single C2B domain. In our model this two-step process is simplified to a single reaction step by taking $[Ca^{2+}]_I$ to the power of two. This simplification is reasonable, because we assumed that syt could only associate to the vesicular membrane when two Ca^{2+} ions are bound, and binding of one Ca^{2+} ion would not induce an 'intermediate' association state to the membrane, nor would it affect the allosteric interaction. By simplifying the two Ca^{2+} binding/ubinding steps to one, we indirectly assumed high cooperativity between the two Ca^{2+} binding sites. To account for the limit on the number of syts bound to $PI(4,5)P_2$, the number of available, empty slots, (M_{slots}-*n-k),* was multiplied on the $PI(4,5)P_2$ binding rates. The fusion rate of the SV is computed by $L_+ \cdot f^n$ (similar to (Lou *et al.*, 2005)), with L_+ denoting the basal fusion rate and *f* the factor of increase in fusion rate by each dual binding being formed. L_+ was set to 4.23e-4 s^{-1} to match the release rate measured at low $[Ca^{2+}]_i$, given an average size of the RRP of 4000 SVs (see below).

The affinities for Ca^{2+} and $PI(4,5)P_2$ binding to syt were set to previously determined dissociation constants ($K_{D,Ca2+}=\beta/\alpha=221^2\ \mu M^2$, $K_{D,PI(4,5)P2}=\delta/\gamma=20\ \mu M$) obtained using *in vitro* microscale thermophoresis experiments (van den Bogaart *et al.*, 2012). For determination of the dissociation constant of Ca^{2+}, van den Bogaart and colleagues assumed binding of a single Ca^{2+} ion to the C2AB domain (van den Bogaart et al., 2012). The $K_{D,2Ca2+}$ of the reaction describing binding of two Ca^{2+} ions, in our model, can be computed from the experimentally derived dissociation constant by taking it to the power of two. This was corroborated by re-fitting the experimental data with a hill coefficient of 2, which yielded a similar $K_{D,2Ca2+}$ value of ~221^2 (data not shown).

751 The *in vitro* experiments revealed a change in syt1 Ca^{2+} affinity upon binding $PI(4,5)P_2$, and vice
752 versa (van den Bogaart et al., 2012), indicating a positive allosteric relationship between the two
753 species. We assumed this allosteric effect was due to a stabilization of the dual-bound state by
754 lowering of the unbinding rates of Ca^{2+} and $PI(4,5)P_2$ with a factor ($A=(3.3/221)^2=0.00022$) and occurs
755 when both species have bound. Upon dual binding, both rate constants for unbinding Ca^{2+} and $PI(4,5)P_2$
756 are multiplied by A, since any closed chemical system must obey microscopic reversibility (Colquhoun
757 et al., 2004). Using the biochemically defined affinities, the number of free parameters in our model
758 was constrained to:

759 $$\xi = (\alpha, \gamma, [PI(4,5)P_2], f)$$

760 The values of β and δ were determined according to the affinities for each choice of α and γ.

761

762 **The steady state of the system**

763 The steady state of the system before stimulation was determined at a resting, global $[Ca^{2+}]_i$ of 0.05
764 µM (except for simulations with Ca^{2+} levels below this basal value, for those we assumed
765 $[Ca^{2+}]_{rest}=[Ca^{2+}]_i$). To compute the steady state, we assumed that no fusion took place, ignoring the very
766 low fusion rate at resting $[Ca^{2+}]_i$. Under these conditions the model is a closed system of recurrent
767 states and obeys microscopic reversibility, i.e. for every closed loop state diagram, the product of the
768 rate constants around the loop is the same in both directions (Colquhoun *et al.*, 2004). Microscopic
769 reversibility implies detailed balance, meaning that every reaction is in equilibrium at steady state.
770 Thus, for any two states S_i and S_j which are connected by a reaction, the steady state distribution obeys

771 $$[S_j] = \frac{r_{ji}}{r_{ij}}[S_i]$$

772 where $[S_i]$ and $[S_j]$ are steady state quantities and r_{ij} and r_{ji} are the reaction rates between S_i and S_j.
773 Using this property, we calculated the steady state iteratively by setting the population of the first
774 state (state (0,0,0)), to 1, and thereafter iteratively computing the population of the following state
775 (following the lexicographic ordering as described above) using the following formula's:

776 $$If\ k > 0: [(n,m,k)] = \frac{r_{k-1,k}}{r_{k,k-1}}[(n,m,k-1)]$$

777 $$If\ m > 0\ and\ k = 0: [(n,m,0)] = \frac{r_{m-1,m}}{r_{m,m-1}}[(n,m-1,0)]$$

778 $$If\ n > 0\ and\ m = k = 0: [(n,0,0)] = \frac{r_{n-1,n}}{r_{n,n-1}}[(n-1,0,0)]$$

Afterwards, each state was divided by the sum of all state values and multiplied by the number of SVs in the RRP. In our model simulations, the size of the RRP was variable and followed a gamma distribution with a mean of 4000 SVs and a standard deviation of 2000 SVs, based on experimental estimates from the calyx of Held (Wölfel and Schneggenburger, 2003). In the following calculations we use φ to denote the steady state probability vector (i.e. normalised the sum to 1).

Computation of fusion probabilities and fusion rate

The analytical implementation of our model allowed us to compute the fusion rate and cumulative fusion probabilities with a constant $[Ca^{2+}]_i$ after stimulus onset (t=0), thereby mimicking conditions in Ca^{2+} uncaging experiments. The constant $[Ca^{2+}]_i$ makes the model a homogenous Markov Model. The transition rates of the model can be organized in the intensity matrix, *Q*, such that,

$$Q_{i,j} = k_{i,j}\ for\ i \neq j$$

$$Q_{i,i} = -\sum_{j \neq i} k_{i,j}$$

where $k_{i,j}$ is the rate of the reaction from state *i* to state *j*. Given initial conditions, φ (steady state normalized to a probability vector), free model parameters, ξ, and calcium concentration, *C,*

$$p_{\xi,C}(t) = \varphi \exp\left(Q_{\xi,C} t\right)$$

is the distribution of SV states a time t, i.e., a $1 \times n_{states}$ vector with element *i* being the probability of being in state *i* at time point *t*. The single SV cumulative fusion probability is the last element, which we will denote with a subscript F,

$$G_{\xi,C}(t) = \left(p_{\xi,C}(t)\right)_F = \left(\varphi \exp\left(Q_{\xi,C} t\right)\right)_F \quad (1)$$

The fusion rate of a single SV can be calculated directly as the last element of the derivative of (1):

$$G'_{\xi,C}(t) = \left(\frac{dp_{\xi,C}(t)}{dt}\right)_F = \left(\varphi\, Q_{\xi,C} \exp\left(Q_{\xi,C} t\right)\right)_F \quad (2)$$

Multiplying (1) and (2) with the number of SVs yields the cumulative fusion function and fusion rate function, respectively. For simulation of peak release rates and release latencies (in Figure 2,4, 5), we computed (1) and (2) using the best fit parameters from fitting with M_{slots}=3 and n_{syts}=15. This was done for 31 $[Ca^{2+}]_i$ values ranging from 0.001 µM to 80 µM (0.001, 0.1, 0.2, …. , 0.9, 1, 1.25, 1.5, 1.75, 2, 2.5, 3, 4, … , 9, 10, 20, 30, …, 80 µM) for $t \in [0,100]$ ms with a time step of 0.01 ms. In addition, the functions were calculated in the same way using the best fit parameters for M_{slots}=1,2,4,5,6 with n_{syts}=15 for

807 simulations depicted in Figure 2A-C. In some conditions, especially at low $[Ca^{2+}]_i$, a longer span of the
808 cumulative fusion probability was required and was calculated with the same time step size.

809

810 **Computation of peak release rates**

811 The peak of the fusion rate can be computed by multiplying the maximum value of the single SV fusion
812 rate function, (2), with n_{ves}. To allow for a variable RRP size, a set of 1000 n_{ves} values were drawn
813 according to the RRP size distribution, the peak release rates were determined, and the mean and 95
814 % prediction interval determined (Figure 2A, 2 supplement 4, 2 supplement 5, 4 supplement 1, 5A, 5
815 supplement 1A) for each Ca^{2+} concentration.

816 For parameter exploration (Figure 2G) and for computing the release rates in the fitting
817 routine, it was not feasible to calculate the fusion rate over 100 ms with high temporal precision.
818 Instead, we implemented a custom search algorithm (scripts can be found in accompanying zip-file
819 "Source_code1.zip"), which was constructed to shorten calculation time by taking advantage of the
820 release rate function being unimodal. We first found a time point, t_{max}, at which 75-90 % of the SVs
821 had fused. Having computed different time points in the time interval $[0,t_{max}]$, gave us an interval in
822 which the fusion rate showed a local maximum. The algorithm then narrowed the time interval down
823 until a time of peak was found with a precision of 0.01 ms. This method shortened simulation time
824 considerably.

825

826 **Stochastic simulation of release latencies**

827 Release latencies (Figure 2A, 2 supplement 4, 2 supplement 5, 4 supplement 1, 5A, 5 supplement 1A),
828 which are defined as the time point of the fifth SV fusion event after the onset of simulation, were
829 simulated stochastically by drawing $p_i \in (0,1)$, $i = 1,\ldots,n_{ves}$, from the uniform distribution for each of the
830 1000 repetitions and each evaluated $[Ca^{2+}]_i$. Each of these random numbers corresponds to the fusion
831 time of an SV, which can be determined using the single SV cumulative fusion probability function (1).
832 To obtain the time point of the fifth SV fusion, the fifth lowest p_i was selected. The corresponding time
833 of fusion was found by interpolation of the single SV cumulative fusion probability, (1). In the
834 corresponding figures, the medians were plotted, since the probability distribution of the release
835 latencies (derived below) was skewed, and the reported data points were single measurements.

836

837 **Fitting the model to experimental data**

838 We next fitted the model to already published data describing the Ca^{2+}-dependence of NT release in
839 the mouse calyx of Held (Kochubey and Schneggenburger, 2011). The data consist of measurements

from Ca^{2+} uncaging experiments, where the release latency, defined as the time point of the fifth SV fusion event, and the peak release rate were estimated at different $[Ca^{2+}]_i$. Besides the four free model parameters, ξ, an additional parameter, *d,* was fitted. *d* is a constant added to the release latencies computed by the model to account for the experimentally observed delay (Kochubey and Schneggenburger, 2011).

Since the variance in the experimental data points also contains information on the underlying biological mechanism, we wanted to take the distribution of individual data points into account when obtaining estimates of the unknown parameters. We therefore derived the likelihood function, which describes how well the model captures the distribution of the release latencies. Obtaining this function for the peak release rates was not feasible. The experimental peak release rates were therefore compared to the average model prediction. Both measures of describing the correspondence between model simulations and experimental data were combined in a cost value which was optimized to estimate the best fit parameters (the lower this cost value the better the correspondence between model predictions and experimental data).

The best fit was obtained by minimizing the following cost function:

$$cost_{\xi,d} = 2 \cdot \sum_{i=1}^{n,rates} S_{\xi,i} - \sum_{j=1}^{n,latencies} \ell_{\xi,d,i}$$

where *i=1,…,* n_{rates} and *j=1,…,* $n_{latencies}$ are the indices of the experimentally measured $[Ca^{2+}]_i$,

$$S_{\xi,i} = \left(r_{max,model} - r_{max,experiment}\right)^2$$

are the squared deviations of the peak release rates ($1/ms^2$) and ℓ is the logarithm of the likelihood of the release latencies (see derivation below). To combine the two measures of distance between model and experimental data, the squared deviation of the peak release rates was multiplied by a factor 2 before subtracting the logarithm of the likelihood of the release latencies. The cost value was minimized using the inbuilt Matlab function *fminsearch,* which uses a Nelder-Mead simplex method. *fminsearch* was run with different initial parameter values to verify that the global minimum of the cost function was found. During the fitting, the lower and upper bounds of *d* were set to, respectively, 0.3 ms and 0.405 ms (with the upper bound corresponding to the smallest release latency in the experimental data set). α,γ, and $[PI(4,5)P_2]$ had an upper bound of 10^{10}, and all free parameters needed to be positive. The maximum number of iterations and function evaluations was set to 5000.

The likelihood function of release latencies with fixed RRP size

To fit the model to the experimental release latency measurements, we derived the likelihood function, which is the probability density function of the model for given parameters evaluated at the experimental data points. Thus, optimizing the likelihood function yields parameters for which the data points are most likely if the model is true. We first derive the likelihood of release latency in the case of a fixed RRP size (n_{ves}).

We define the stochastic variable X, which describes the stochastic process of the state of a single SV in our model. The fusion time of the SV, τ, is defined as

$$\tau = \inf\{t > 0 | X(t) = F\}$$

where τ itself is a stochastic variable. We define a stochastic vector, Z, which consists of all n_{ves} fusion time points in a single experiment. They come from independent, identically distributed stochastic processes with cumulative distribution function $G_{\xi,C}(t)$, given in (1). As the release latency is defined as the time of the fifth SV fusion, we order the Z variable outcomes ($z_{(1)}, z_{(2)}, \dots, z_{(nves)}$) from first to last fusion time. Using the transformation

$$U_{(i)} = G_{\xi,C}\left(Z_{(i)}\right)$$

we obtain a sequence of stochastic variables, $U_{(i)}$, which are uniformly distributed on the interval (0,1). The ordering is preserved, since $G_{\xi,C}(t)$ is monotonically increasing, and U has probability density function

$$f_{U_i}(t) = \left|G'_{\xi,C}\left(Z_{(i)}\right)\right|$$

with respect to t. $G_{\xi,C}'(t) \geq 0$ is given in (2). From order statistics it follows that the kth ordered U is beta-distributed with probability density

$$f_{U_{(k)}}(u) = G_{\xi,C}{}'\left(G_{\xi,C}^{-1}(u)\right) \cdot \frac{n_{ves}!}{(k-1)!\,(n_{ves}-k)!} u^{k-1}(1-u)^{n_{ves}-k}$$

where $u = G_{\xi,C}(t)$. Thus, the transformed variable $U_{(k)}$, is beta-distributed, with

$$U_{(k)} \sim \mathrm{Beta}(k, n_{ves} + 1 - k)$$

In the case of the release latency, we are interested in the fifth fusion event ($k=5$). Thus, with a fixed RRP size, the likelihood value for the release latency observations, $T^*=(t^*_1, t^*_2, \dots, t^*_M)$, at all M Ca^{2+} concentrations is

$$\mathcal{L}_\xi(T^*) = \prod_{i=1}^{M} G_{\xi,C_i}{}'(t_i^*) \frac{n_{ves}!}{4!\,(n_{ves}-5)!} G_{\xi,C_i}(t_i^*)^4 \left(1 - G_{\xi,C_i}(t_i^*)\right)^{n_{ves}-5}$$

In the optimization we minimize minus the log-likelihood:

$$\ell_\xi(T^*) = -\log(\mathcal{L}_\xi(T^*) = -\sum_{i=1}^{M}\left(\log G_{\xi,C_i}{}'(t_i^*)\frac{n_{ves}!}{4!\,(n_{ves}-5)!}G_{\xi,C_i}(t_i^*)^4\left(1-G_{\xi,C_i}(t_i^*)\right)^{n_{ves}-5}\right)$$

which is equivalent to maximizing the likelihood function.

The likelihood of release latencies with variable RRP size

In our model, the RRP size is assumed to follow a Gamma distribution. Let *x* denote the RRP size, $f_{RRP}(x)$ the probability density of the Gamma distribution, and $u= G_{\xi C}(t)$. The probability density of the release latency at Ca^{2+} concentration C_i is given by

$$\tilde{f}_{U_{(k)}}(u) = \frac{1}{K}\int_5^\infty f_{RRP}(x)\,G_{\xi,C_i}{}'\left(G_{\xi,C_i}^{-1}(u)\right)\cdot\frac{x!}{4!\,(x-5)!}u^4(1-u)^{x-5}dx$$

$$= \frac{G_{\xi,C}{}'\left(G_{\xi,C}^{-1}(u)\right)}{K}\int_5^\infty f_{RRP}(x)\cdot\frac{x(x-1)(x-2)(x-3)(x-4)}{4!}u^4e^{\log(1-u)x}e^{-5\log(1-u)}dx \quad (3)$$

where *K* is a normalization constant, K=1-P(x<5)≈1. The lower limit of the integral reflects that the release latency is only defined when there are more than 5 SVs in the RRP. In simulations this corresponds to redrawing the RRP size whenever an RRP size < 5 SVs occurs, which happens with probability ~3e-11, and is accounted for in the normalization constant K in the following. Inserting the probability density function of a Gamma distribution with shape parameter *k* and scale parameter θ, we get:

$$\tilde{f}_{U_{(k)}}(u) = \frac{G_{\xi,C}{}'\left(G_{\xi,C}^{-1}(u)\right)}{K}\int_5^\infty \frac{1}{\Gamma(k)\theta^k}\cdot x^{k-1}\cdot e^{\frac{-x}{\theta}}$$

$$\cdot\frac{x(x-1)(x-2)(x-3)(x-4)}{4!}u^4e^{\log(1-u)x}e^{-5\log(1-u)}dx$$

We now define the following variables:

$$\tilde{\theta} = \frac{\theta}{1-\theta\log(1-u)}, \qquad a = \frac{u^4e^{-5\log(1-u)}G_{\xi,C}{}'\left(G_{\xi,C}^{-1}(u)\right)}{4!\,(1-\theta\log(1-u))^k} \quad (4)$$

By factoring out and substituting in the above equation we get

$$K\tilde{f}_{U_{(k)}}(u) = \frac{G_{\xi,C}{}'\left(G_{\xi,C}^{-1}(u)\right)u^4e^{-5(1-u)}}{4!\,(1-\theta\log(1-u))^k}\int_5^\infty\frac{(1-\theta\log(1-u))^k}{\Gamma(k)\theta^k}\cdot x^{k-1}\cdot e^{\frac{-(1-\theta\log(1-u))x}{\theta}}$$

$$\cdot\, x(x-1)(x-2)(x-3)(x-4)dx$$

$$== a\int_5^\infty\frac{1}{\Gamma(k)\tilde{\theta}^k}\cdot x^{k-1}\cdot e^{\frac{-x}{\tilde{\theta}}}\cdot x(x-1)(x-2)(x-3)(x-4)dx \quad (5)$$

Furthermore, we have

$$x(x-1)(x-2)(x-3)(x-4) = x^5 - 10x^4 + 35x^3 - 50x^2 + 24x \quad (6)$$

Since

$$\Gamma(x+1) = x\Gamma(x)$$

we can derive the following useful formula:

$$I_n = \int_5^\infty \frac{1}{\Gamma(k)\tilde{\theta}^k} \cdot x^{k-1} \cdot e^{\frac{-x}{\tilde{\theta}}} \cdot x^n dx$$

$$= \left(\prod_{m=0}^{n-1} k+m\right) \tilde{\theta}^n \int_5^\infty \frac{1}{\Gamma(k+n)\tilde{\theta}^{k+n}} \cdot x^{k+n-1} \cdot e^{\frac{-x}{\tilde{\theta}}} dx$$

$$= \left(\prod_{m=0}^{n-1} k+m\right) \tilde{\theta}^n \left(1 - \frac{1}{\Gamma(k+n)} \gamma\left(k+n, \frac{5}{\tilde{\theta}}\right)\right) \quad (7)$$

The third equality follows from the fact that the function in the second integral from above is the probability density function of a gamma distribution with shape parameter *k+n* and scale parameter $\tilde{\theta}$. We therefore replace it with the cumulative distribution function of the gamma distribution, where γ is the lower incomplete gamma function. Combining (4), (5), (6), and (7) yields an explicit expression of the likelihood of a single delay in (3), as

$$\tilde{f}_{U_{(k)}}(u) = \frac{a \cdot (I_5 - 10I_4 + 35I_3 - 50I_2 + 24I_1)}{K}$$

with

$$K = 1 - P(x < 5) = 1 - \frac{1}{\Gamma(k)} \gamma\left(k, \frac{5}{\theta}\right)$$

We then minimize the sum of minus the log-likelihoods of the release latency observations.

Syt binding states in the Gillespie simulation of model

In the Gillespie algorithm, the binding state of each individual syt is tracked. The state of the system at time point *t*, *X(t)*, is given by a n_{syt} x n_{ves} matrix. Each element in this matrix describes the binding state of an individual syt using a 2-digit coding system; 00 for no species bound to syt, 01 for PI(4,5)P_2 bound, 10 for two Ca^{2+} ions bound, and 11 for both species bound (dual-binding syt). As with the analytical implementation, each syt can undergo in total 8 different (un)binding reactions (Figure 1A), depending

on the binding state of the respective syt. The fusion rate, which depends on the number of dual-bound syts per SV, is determined for the entire SV.

Determining the initial state of the system

The steady state (initial state, *X(0)*) was computed using the same method as described above (see section '*The steady state of the system*') using $[Ca^{2+}]_i$ = 0.05 µM as the resting condition. This resulted in φ, the probability vector of a single SV to be in the different SV-states at steady state. To stochastically determine *X(0)*, we first determined the binding state for each SV, *i.e.* how many dual bindings are formed (*n)* and how many syts have bound Ca^{2+} (*m)* and how many $PI(4,5)P_2$ (*k)*. For that we drew $p_j \in (0,1)$, $j = 1\ldots,n_{ves}$, from the uniform distribution. The state number of the jth SV, *s*, was determined by:

$$s = \text{smallest integer satisfying } \sum_{i=1}^{s} \varphi_i \geq p_j$$

Via the ordering of states explained above, *s* can be linked to the state triplet (n_s,m_s,k_s). As the order of syts is irrelevant for model simulation, this information on the state of SV_j was transferred to the jth column of the *X(0)* matrix in a systematic way: The first n_s elements were labeled with '11'; elements n_s+1 to n_s+m_s were labeled with '10'; and elements n_s+m_s+1 to $n_s+m_s+k_s$ were labeled with '01', and the remaining elements $(n_s+m_s+k_s+1):n_{syt}$ were set to '00'.

Gillespie algorithm-based simulations of the model

For stochastic evaluation of the model by the Gillespie algorithm (Gillespie, 2007), we next introduced the propensity function *b*, which is defined by:

$b_{i,j}(x)dt :=$ the probability given *(X(t) = X)*, that the ith syt of the jth SV will undergo a reaction in the next infinitesimal time interval [*t, t+dt*].

For element *i,j* in *b*, the total reaction propensity is the sum of propensities of possible reactions given the binding state of the syt and can be computed as follow:

$$b_{i,j}(X_{i,j}) = \begin{cases} \max\left(M_{slots} - PIP_{tot,j}, 0\right)\gamma\,[PI(4,5)P_2] + \alpha[Ca^{2+}]^2, & X_{i,j} = 00 \\ \delta + \alpha[Ca^{2+}]^2, & X_{i,j} = 01 \\ \beta + \max\left(M_{slots} - PIP_{tot,j}, 0\right)\gamma\,[PI(4,5)P_2], & X_{i,j} = 10 \\ A\delta + A\beta, & X_{i,j} = 11 \end{cases}$$

with $PIP_{tot,j}$ the total number of syts of SV *j* bound to $PI(4,5)P_2$. To include the propensity for fusion of an SV, an additional row in *b*, b_f, describes the propensity of fusion for each SV in the matrix;

$$b_{f,j} = l_{+} f^{\sum_{i=1}^{n_{syt}} \mathbf{1}_{(X_{i,j}=11)}}$$

This makes b a matrix of $(n_{syt}+1) \times n_{ves}$. We denote the sum of all elements in b by b_0. Using b_0 and 3 random numbers ($r_n \in (0,1)$, $n = 1,2,3$) drawn from the uniform distribution, we determined the time step to the next reaction and which SV and syt this reaction affects. The time to next reaction, τ, is given by

$$\tau = \frac{1}{b_0} \ln\left(\frac{1}{r_1}\right)$$

since it is exponentially distributed with rate b_0. The index, j, of the SV undergoing a reaction is the first index that satisfies:

$$\sum_{j'=1}^{j} \sum_{i=1}^{n_{syt}+1} b_{i,j'} \geq r_2\, b_0$$

Similarly, the index i of the syt in SV j undergoing a reaction is the smallest integer fulfilling:

$$\sum_{i'=1}^{i} b_{i',j} \geq r_3 \sum_{\hat{\imath}=1}^{n_{syt}+1} b_{\hat{\imath},j}$$

If the row index i equals n_{syt}+1, a fusion reaction occurs. The fusion time ($t + \tau$) is saved and all the propensities of SV j in b are set to 0. If i is smaller or equal to n_{syt} a binding or unbinding reaction of one of the two species occurs. To determine which of the four possible reactions is occurring, we define an additional propensity matrix, b_{react}. The first element in b_{react} denotes the propensity of PI(4,5)P_2 binding, the second element the propensity of Ca^{2+} binding, and the third and fourth element the unbinding of PI(4,5)P_2 and Ca^{2+}, respectively. These elements are given by:

$$b_{react,1} = \mathbf{1}_{(X_{i,j}=00 \vee x_{i,j}=10)} \max\left(M_{slots} - PIP_{tot,j}, 0\right) \gamma\, [PI(4,5)P_2]$$

$$b_{react,2} = \mathbf{1}_{(X_{i,j}=00 \vee X_{i,j}=01)}\, \alpha [Ca^{2+}]^2$$

$$b_{react,3} = \mathbf{1}_{(X_{i,j}=01 \vee X_{i,j}=11)}\, A^{\mathbf{1}_{(X_{i,j}=11)}} \delta$$

$$b_{react,4} = \mathbf{1}_{(X_{i,j}=10 \vee X_{i,j}=11)}\, A^{\mathbf{1}_{(X_{i,j}=11)}} \beta$$

Additionally, we define the transition matrix V, which describes the change in the state of $X_{i,j}$ induced by the four reactions:

$$V = (+01, +10, -01, -10)$$

A fourth random number, $r_4 \in (0,1)$, drawn from the uniform distribution, determines which reaction occurs via:

h = smallest integer satisfying $\sum_{h'=1}^{h} b_{react,h'} \geq r_4 \sum_{\hat{h}=1}^{4} b_{react,\hat{h}}$

The state of the corresponding SV and syt, $X_{i,j,}$ is replaced by $X_{i,j} + V_h$ and t by $t + \tau$. Then b is updated according to the change in X, and all steps are repeated. This iterative process continues until all SVs are fused, when simulating the model with a fixed $[Ca^{2+}]_i$.

When simulating AP-evoked responses (Figure 5, Figure 6), we used a Ca^{2+} transient describing the microdomain $[Ca^{2+}]_i$ sensed locally by primed SVs in the mouse calyx of Held upon AP stimulation (Wang *et al.*, 2008). This Ca^{2+} transient also formed the basis for the Ca^{2+} signal used to simulate a paired pulse stimulus (Figure 7), where the transients were placed with a 10 ms interval. Additionally, for the paired pulse stimulus, we added a residual Ca^{2+}-transient to the signal (exponential decay with amplitude: 0.4 µM, decay time constant: 0.154 s^{-1}). Similar to the uncaging simulations, the $[Ca^{2+}]_i$ before the onset of the stimulus was 0.05µM. Since the Ca^{2+} concentration is a factor in the reaction rates, the propensity matrices b and b_{react} were not only updated to the new state matrix, $X(t + \tau)$, but also to a new $[Ca^{2+}]_i$ at time $t + \tau$. $[Ca^{2+}]$ at time $t + \tau$ was determined from the Ca^{2+} transient using linear interpolation, and b and b_{react} were updated correspondingly. As the propensity of Ca^{2+} binding is largely dependent on $[Ca^{2+}]_i$, the time step between two updates in $[Ca^{2+}]_{curr}$ and the propensity matrices was set to be at most $8e^{-4}$s. If τ determined from b at time t was larger than this time step, no reaction occurred, but the system and $[Ca^{2+}]_{curr}$ were updated to time t+$8e^{-4}$s. The model was evaluated until the end of the Ca^{2+} transient. Similarly, in the case of a variable $PI(4,5)P_2$ transient (Figure 7), the $PI(4,5)P_2$ concentration was updated at least every $8e^{-4}$s. Because this approach requires simulation of all individual (un)binding reactions and fusion events it is not feasible to perform 1000 repetitions. Instead, simulations were repeated 200 times (Figure 5, 6). Like with the computation of the release latencies and maximal fusion rates, we assumed a variable RRP. However, instead of drawing random pool sizes from a gamma distribution, we used the 200 quantiles of the pdf of the RRP sizes, because of the limited number of repetitions and the large impact of the RRP size on the model predictions. In Figure 7, we reduced the number of repetitions to 50, to represent an experimental condition more closely. The RRP was drawn randomly once. This set of random RRP values was used for both the mutant and the WT condition displayed in the figure.

Simulating the model with mutant syts

For mutations in syt that affect the binding and unbinding rates of $PI(4,5)P_2$ and Ca^{2+}, the procedure described above was repeated with adjusted parameters when simulating a model containing only

1032 mutant syts. For a model in which mutant proteins were expressed together with WT syts (simulations
1033 of heterozygous condition in Figure 6), the procedure was changed slightly.

1034 For a model with *p* WT and *q* mutant syts, the number of states of an SV increases drastically
1035 and was now described by six values; the number of WT syts bound to Ca^{2+}, PI(4,5)P_2 or both, and the
1036 number of mutant syts bound to Ca^{2+}, PI(4,5)P_2 or both. The dimensions of the Q-matrix used to
1037 compute the steady-state probability of a single SV increased proportionally with n_{states}. *X(t=0)* was
1038 computed using the same principle as described above, with the important difference that the first *p*
1039 rows represented the binding status of the WT syts, and row *p+1:p+q* that of the mutants. In *b* this
1040 ordering of WT and mutant syts is the same. The parameters used to compute b_{react} depended on
1041 whether a reaction occurred to a WT syt, $i \leq p$, or a mutant syt, $n_{syt} \geq i > p$.

1042

1043 **Simulation of EPSCs**

1044 Simulated EPSCs were obtained using both model implementations. The analytical implementation of
1045 our model was used to simulate fusion times for a constant $[Ca^{2+}]_i$ (Figure 4D,G). The Gillespie version
1046 of the model was used to simulate AP-evoked EPSCs with or without mutant syts (Figure 5C-E, Figure
1047 5 - figure supplement 1E-F, Figure 6C-D, 6 supplement 1, and 7B-D-E). In both approaches the
1048 stochastically determined fusion times, determined as described above, were rounded up to the next
1049 0.02 ms, leading to a sampling rate of 50 kHz. The sampled fusion times were convolved with a mEPSC
1050 to generate simulated EPSCs. The standard mEPSC used for deconvolution followed the equation
1051 described by Neher and Sakaba (Neher and Sakaba, 2001):

1052 $$I_{mini}(t) = A \cdot (1-\rho)\exp\left(-\frac{t}{\tau_1}\right) + \rho \cdot \exp\left(-\frac{t}{\tau_2}\right) - \exp\left(-\frac{t}{\tau_0}\right)$$

1053 with τ_1 = 0.12 ms (time constant of fast decay), τ_2 = 13 ms (time constant of slow decay), τ_0 = 0.12 ms
1054 (time constant of rise phase), ρ = 1.e-5 (proportion of slow phase in decay), and *A* being a normalization
1055 constant making the amplitude 60 pA. Parameter values were chosen such that the kinetics of the
1056 mEPSC would match events measured in the Calyx of Held (Chang et al., 2015). In Figure 4D,G traces
1057 show three randomly chosen eEPSCs in each panel. Representative eEPSC traces shown in Figures 5,
1058 6, 6 supplement 1, and 7 are simulated eEPSCs with the amplitude closest to the mean eEPSC
1059 amplitude.

1060

1061 **Simulating AP-evoked EPSCs with variable syt**

To investigate the effect of variability in the number of syts expressed per SV on variance between simulated AP-evoked traces model (Figure 5), we first had to determine the steady state. For this we computed the probability vector of a single SV to be in the different SV-states at steady state (φ) for n_{syt}=1,…,50. Subsequently, for each SV and each repetition (n=1000) a random number of n_{syt} was drawn from the Poisson distribution with mean=15. When the value 0 was drawn, it was replaced by n_{syt}=1. Using these values and φ determined for each n_{syt}, we computed the steady state matrix (X(0)) as described above ("Determining the initial state of the system"). To reduce computation time, we evaluated a model containing 100 vesicles 40 times instead of evaluating 4000 vesicles simultaneously. The fusion times obtained when driving the model with the Ca^{2+}-transient were combined afterwards. This is valid since all SVs act independently in the model. For the condition with a variable RRP size, fusion times were selected randomly until the RRP size of that specific repetition was reached. Afterwards, the fusion times were convolved with the mEPSC to obtain simulated AP-evoked responses. To quantify the variance in the traces, we computed the standard deviation of the simulated eEPSCs at each data point (300 data points corresponding to the time interval 0-6ms) and summed those values.

Acknowledgements

We would like to thank Ralf Schneggenburger and Holger Taschenberger for providing the experimental Ca^{2+} uncaging dataset and AP-induced Ca^{2+} transient. This work was supported by grants from the Deutsche Forschungsgemeinschaft (Emmy Noether Programme, Project Number 261020751 and the TRR 186, Project Number 278001972 to A.M.W), the Novo Nordisk Foundation (NNF20OC0062958 to S.D.; NNF19OC0058298 to J.B.S and a Young Investigator Award NNF19OC0056047 to A.M.W.), the Lundbeck Foundation (R277-2018-802 to J.B.S.) and the Independent Research Fund Denmark (8020-00228A to J.B.S.).

Competing Interests

The authors declare no conflicting financial and non-financial interest.

Additional files

Supplementary files:

- “Source_code1.zip”: MATLAB scripts used for simulations.
- Transparent reporting form
- Source data files for all figures and figure supplements

References

Abbott, L.F., and Regehr, W.G. (2004). Synaptic computation. Nature *431*, 796-803. 10.1038/nature03010.

Araç, D., Chen, X., Khant, H.A., Ubach, J., Ludtke, S.J., Kikkawa, M., Johnson, A.E., Chiu, W., Südhof, T.C., and Rizo, J. (2006). Close membrane-membrane proximity induced by Ca2+-dependent multivalent binding of synaptotagmin-1 to phospholipids. Nature structural & molecular biology *13*, 209-217. 10.1038/nsmb1056.

Arancillo, M., Min, S.W., Gerber, S., Münster-Wandowski, A., Wu, Y.J., Herman, M., Trimbuch, T., Rah, J.C., Ahnert-Hilger, G., Riedel, D., et al. (2013). Titration of Syntaxin1 in mammalian synapses reveals multiple roles in vesicle docking, priming, and release probability. J Neurosci *33*, 16698-16714. 10.1523/jneurosci.0187-13.2013.

Bacaj, T., Wu, D., Yang, X., Morishita, W., Zhou, P., Xu, W., Malenka, R.C., and Sudhof, T.C. (2013). Synaptotagmin-1 and synaptotagmin-7 trigger synchronous and asynchronous phases of neurotransmitter release. Neuron *80*, 947-959. 10.1016/j.neuron.2013.10.026.

Bai, J., Tucker, W.C., and Chapman, E.R. (2004). PIP2 increases the speed of response of synaptotagmin and steers its membrane-penetration activity toward the plasma membrane. Nature structural & molecular biology *11*, 36-44. 10.1038/nsmb709.

Bhalla, A., Chicka, M.C., Tucker, W.C., and Chapman, E.R. (2006). Ca(2+)-synaptotagmin directly regulates t-SNARE function during reconstituted membrane fusion. Nature structural & molecular biology *13*, 323-330. 10.1038/nsmb1076.

Bollmann, J.H., Sakmann, B., and Borst, J.G. (2000). Calcium sensitivity of glutamate release in a calyx-type terminal. Science (New York, N.Y.) *289*, 953-957.

Bowers, M.R., and Reist, N.E. (2020). The C2A domain of synaptotagmin is an essential component of the calcium sensor for synaptic transmission. PloS one *15*, e0228348. 10.1371/journal.pone.0228348.

Bradberry, M.M., Courtney, N.A., Dominguez, M.J., Lofquist, S.M., Knox, A.T., Sutton, R.B., and Chapman, E.R. (2020). Molecular Basis for Synaptotagmin-1-Associated Neurodevelopmental Disorder. Neuron *107*, 52-64 e57. 10.1016/j.neuron.2020.04.003.

Brewer, K.D., Bacaj, T., Cavalli, A., Camilloni, C., Swarbrick, J.D., Liu, J., Zhou, A., Zhou, P., Barlow, N., Xu, J., et al. (2015). Dynamic binding mode of a Synaptotagmin-1-SNARE complex in solution. Nature structural & molecular biology *22*, 555-564. 10.1038/nsmb.3035.

Burgalossi, A., Jung, S., Meyer, G., Jockusch, W.J., Jahn, O., Taschenberger, H., O'Connor, V.M., Nishiki, T., Takahashi, M., Brose, N., and Rhee, J.S. (2010). SNARE protein recycling by alphaSNAP and betaSNAP supports synaptic vesicle priming. Neuron *68*, 473-487. 10.1016/j.neuron.2010.09.019.

Chang, S., Reim, K., Pedersen, M., Neher, E., Brose, N., and Taschenberger, H. (2015). Complexin stabilizes newly primed synaptic vesicles and prevents their premature fusion at the mouse calyx of held synapse. J Neurosci *35*, 8272-8290. 10.1523/JNEUROSCI.4841-14.2015.

Chang, S., Trimbuch, T., and Rosenmund, C. (2018). Synaptotagmin-1 drives synchronous Ca(2+)-triggered fusion by C2B-domain-mediated synaptic-vesicle-membrane attachment. Nature neuroscience *21*, 33-40. 10.1038/s41593-017-0037-5.

Chen, Y., Wang, Y.H., Zheng, Y., Li, M., Wang, B., Wang, Q.W., Fu, C.L., Liu, Y.N., Li, X., and Yao, J. (2021). Synaptotagmin-1 interacts with PI(4,5)P2 to initiate synaptic vesicle docking in hippocampal neurons. Cell Rep *34*, 108842. 10.1016/j.celrep.2021.108842.

Colquhoun, D., Dowsland, K.A., Beato, M., and Plested, A.J. (2004). How to impose microscopic reversibility in complex reaction mechanisms. Biophysical journal *86*, 3510-3518. 10.1529/biophysj.103.038679.

Courtney, N.A., Bao, H., Briguglio, J.S., and Chapman, E.R. (2019). Synaptotagmin 1 clamps synaptic vesicle fusion in mammalian neurons independent of complexin. Nat Commun *10*, 4076. 10.1038/s41467-019-12015-w.

de Wit, H., Walter, A.M., Milosevic, I., Gulyas-Kovacs, A., Riedel, D., Sorensen, J.B., and Verhage, M. (2009). Synaptotagmin-1 docks secretory vesicles to syntaxin-1/SNAP-25 acceptor complexes. Cell *138*, 935-946. 10.1016/j.cell.2009.07.027.

Dittrich, M., Pattillo, J.M., King, J.D., Cho, S., Stiles, J.R., and Meriney, S.D. (2013). An excess-calcium-binding-site model predicts neurotransmitter release at the neuromuscular junction. Biophysical journal *104*, 2751-2763. 10.1016/j.bpj.2013.05.023.

Fernandez-Chacon, R., Konigstorfer, A., Gerber, S.H., Garcia, J., Matos, M.F., Stevens, C.F., Brose, N., Rizo, J., Rosenmund, C., and Sudhof, T.C. (2001). Synaptotagmin I functions as a calcium regulator of release probability. Nature *410*, 41-49. 10.1038/35065004.

Fernández-Chacón, R., Shin, O.H., Königstorfer, A., Matos, M.F., Meyer, A.C., Garcia, J., Gerber, S.H., Rizo, J., Südhof, T.C., and Rosenmund, C. (2002). Structure/function analysis of Ca2+ binding to the C2A domain of synaptotagmin 1. J Neurosci *22*, 8438-8446. 10.1523/jneurosci.22-19-08438.2002.

Fernandez, I., Arac, D., Ubach, J., Gerber, S.H., Shin, O., Gao, Y., Anderson, R.G., Sudhof, T.C., and Rizo, J. (2001). Three-dimensional structure of the synaptotagmin 1 C2B-domain: synaptotagmin 1 as a phospholipid binding machine. Neuron *32*, 1057-1069. 10.1016/s0896-6273(01)00548-7.

Geppert, M., Goda, Y., Hammer, R.E., Li, C., Rosahl, T.W., Stevens, C.F., and Sudhof, T.C. (1994). Synaptotagmin I: a major Ca2+ sensor for transmitter release at a central synapse. Cell *79*, 717-727.

Gillespie, D.T. (2007). Stochastic Simulation of Chemical Kinetics. Annual Review of Physical Chemistry *58*, 35-55. 10.1146/annurev.physchem.58.032806.104637.

Gruget, C., Bello, O., Coleman, J., Krishnakumar, S.S., Perez, E., Rothman, J.E., Pincet, F., and Donaldson, S.H., Jr. (2020). Synaptotagmin-1 membrane binding is driven by the C2B domain and assisted cooperatively by the C2A domain. Sci Rep *10*, 18011. 10.1038/s41598-020-74923-y.

Gruget, C., Coleman, J., Bello, O., Krishnakumar, S.S., Perez, E., Rothman, J.E., Pincet, F., and Donaldson, S.H., Jr. (2018). Rearrangements under confinement lead to increased binding energy of Synaptotagmin-1 with anionic membranes in Mg(2+) and Ca(2). FEBS Lett *592*, 1497-1506. 10.1002/1873-3468.13040.

Guan, Z., Bykhovskaia, M., Jorquera, R.A., Sutton, R.B., Akbergenova, Y., and Littleton, J.T. (2017). A synaptotagmin suppressor screen indicates SNARE binding controls the timing and Ca(2+) cooperativity of vesicle fusion. Elife *6*. 10.7554/eLife.28409.

Heidelberger, R., Heinemann, C., Neher, E., and Matthews, G. (1994). Calcium dependence of the rate of exocytosis in a synaptic terminal. Nature *371*, 513-515. 10.1038/371513a0.

Helmchen, F., Borst, J.G., and Sakmann, B. (1997). Calcium dynamics associated with a single action potential in a CNS presynaptic terminal. Biophysical journal *72*, 1458-1471. 10.1016/s0006-3495(97)78792-7.

Honigmann, A., van den Bogaart, G., Iraheta, E., Risselada, H.J., Milovanovic, D., Mueller, V., Mullar, S., Diederichsen, U., Fasshauer, D., Grubmuller, H., et al. (2013). Phosphatidylinositol 4,5-bisphosphate clusters act as molecular beacons for vesicle recruitment. Nature structural & molecular biology *20*, 679-686. 10.1038/nsmb.2570.

Hui, E., Gaffaney, J.D., Wang, Z., Johnson, C.P., Evans, C.S., and Chapman, E.R. (2011). Mechanism and function of synaptotagmin-mediated membrane apposition. Nature structural & molecular biology *18*, 813-821. 10.1038/nsmb.2075.

Imig, C., Min, S.W., Krinner, S., Arancillo, M., Rosenmund, C., Sudhof, T.C., Rhee, J., Brose, N., and Cooper, B.H. (2014). The morphological and molecular nature of synaptic vesicle priming at presynaptic active zones. Neuron *84*, 416-431. 10.1016/j.neuron.2014.10.009.

Jackman, S.L., Turecek, J., Belinsky, J.E., and Regehr, W.G. (2016). The calcium sensor synaptotagmin 7 is required for synaptic facilitation. Nature *529*, 88-91. 10.1038/nature16507.

Jahn, R., and Fasshauer, D. (2012). Molecular machines governing exocytosis of synaptic vesicles. Nature *490*, 201-207. 10.1038/nature11320.

Kaeser, P.S., and Regehr, W.G. (2017). The readily releasable pool of synaptic vesicles. Curr Opin Neurobiol *43*, 63-70. 10.1016/j.conb.2016.12.012.

Kedar, G.H., Munch, A.S., van Weering, J.R., Malsam, J., Scheutzow, A., de Wit, H., Houy, S., Tawfik, B., Söllner, T.H., Sørensen, J.B., and Verhage, M. (2015). A Post-Docking Role of Synaptotagmin 1-C2B Domain Bottom Residues R398/399 in Mouse Chromaffin Cells. J Neurosci *35*, 14172-14182. 10.1523/jneurosci.1911-15.2015.

1198 Kobbersmed, J.R., Grasskamp, A.T., Jusyte, M., Bohme, M.A., Ditlevsen, S., Sorensen, J.B., and Walter,
1199 A.M. (2020). Rapid regulation of vesicle priming explains synaptic facilitation despite heterogeneous
1200 vesicle:Ca(2+) channel distances. Elife *9*. 10.7554/eLife.51032.
1201 Kochubey, O., Babai, N., and Schneggenburger, R. (2016). A Synaptotagmin Isoform Switch during the
1202 Development of an Identified CNS Synapse. Neuron *90*, 984-999. 10.1016/j.neuron.2016.04.038.
1203 Kochubey, O., and Schneggenburger, R. (2011). Synaptotagmin Increases the Dynamic Range of
1204 Synapses by Driving Ca2+-Evoked Release and by Clamping a Near-Linear Remaining Ca2+ Sensor.
1205 Neuron *69*, 736-748. 10.1016/j.neuron.2011.01.013.
1206 Kusick, G.F., Chin, M., Raychaudhuri, S., Lippmann, K., Adula, K.P., Hujber, E.J., Vu, T., Davis, M.W.,
1207 Jorgensen, E.M., and Watanabe, S. (2020). Synaptic vesicles transiently dock to refill release sites.
1208 Nature neuroscience *23*, 1329-1338. 10.1038/s41593-020-00716-1.
1209 Lai, A.L., Tamm, L.K., Ellena, J.F., and Cafiso, D.S. (2011). Synaptotagmin 1 modulates lipid acyl chain
1210 order in lipid bilayers by demixing phosphatidylserine. The Journal of biological chemistry *286*, 25291-
1211 25300. 10.1074/jbc.M111.258848.
1212 Lee, J., Guan, Z., Akbergenova, Y., and Littleton, J.T. (2013). Genetic analysis of synaptotagmin C2
1213 domain specificity in regulating spontaneous and evoked neurotransmitter release. J Neurosci *33*, 187-
1214 200. 10.1523/JNEUROSCI.3214-12.2013.
1215 Li, F., Tiwari, N., Rothman, J.E., and Pincet, F. (2016). Kinetic barriers to SNAREpin assembly in the
1216 regulation of membrane docking/priming and fusion. Proceedings of the National Academy of Sciences
1217 of the United States of America *113*, 10536-10541. 10.1073/pnas.1604000113.
1218 Li, L., Shin, O.H., Rhee, J.S., Arac, D., Rah, J.C., Rizo, J., Sudhof, T., and Rosenmund, C. (2006).
1219 Phosphatidylinositol phosphates as co-activators of Ca2+ binding to C2 domains of synaptotagmin 1.
1220 The Journal of biological chemistry *281*, 15845-15852. 10.1074/jbc.M600888200.
1221 Lin, C.C., Seikowski, J., Perez-Lara, A., Jahn, R., Hobartner, C., and Walla, P.J. (2014). Control of
1222 membrane gaps by synaptotagmin-Ca2+ measured with a novel membrane distance ruler. Nat
1223 Commun *5*, 5859. 10.1038/ncomms6859.
1224 Littleton, J.T., Stern, M., Schulze, K., Perin, M., and Bellen, H.J. (1993). Mutational analysis of Drosophila
1225 synaptotagmin demonstrates its essential role in Ca(2+)-activated neurotransmitter release. Cell *74*,
1226 1125-1134. 10.1016/0092-8674(93)90733-7.
1227 Liu, X., Seven, A.B., Camacho, M., Esser, V., Xu, J., Trimbuch, T., Quade, B., Su, L., Ma, C., Rosenmund,
1228 C., and Rizo, J. (2016). Functional synergy between the Munc13 C-terminal C1 and C2 domains. Elife *5*.
1229 10.7554/eLife.13696.
1230 Lou, X., Scheuss, V., and Schneggenburger, R. (2005). Allosteric modulation of the presynaptic Ca2+
1231 sensor for vesicle fusion. Nature *435*, 497-501. 10.1038/nature03568.
1232 Luo, F., and Sudhof, T.C. (2017). Synaptotagmin-7-Mediated Asynchronous Release Boosts High-
1233 Fidelity Synchronous Transmission at a Central Synapse. Neuron *94*, 826-839 e823.
1234 10.1016/j.neuron.2017.04.020.
1235 Ma, L., Cai, Y., Li, Y., Jiao, J., Wu, Z., O'Shaughnessy, B., De Camilli, P., Karatekin, E., and Zhang, Y. (2017).
1236 Single-molecule force spectroscopy of protein-membrane interactions. Elife *6*. 10.7554/eLife.30493.
1237 Mackler, J.M., Drummond, J.A., Loewen, C.A., Robinson, I.M., and Reist, N.E. (2002). The C(2)B Ca(2+)-
1238 binding motif of synaptotagmin is required for synaptic transmission in vivo. Nature *418*, 340-344.
1239 10.1038/nature00846.
1240 Mackler, J.M., and Reist, N.E. (2001). Mutations in the second C2 domain of synaptotagmin disrupt
1241 synaptic transmission at Drosophila neuromuscular junctions. The Journal of comparative neurology
1242 *436*, 4-16.
1243 Martens, S., Kozlov, M.M., and McMahon, H.T. (2007). How synaptotagmin promotes membrane
1244 fusion. Science (New York, N.Y.) *316*, 1205-1208. 10.1126/science.1142614.
1245 Miki, T., Malagon, G., Pulido, C., Llano, I., Neher, E., and Marty, A. (2016). Actin- and Myosin-Dependent
1246 Vesicle Loading of Presynaptic Docking Sites Prior to Exocytosis. Neuron *91*, 808-823.
1247 10.1016/j.neuron.2016.07.033.

Milosevic, I., Sørensen, J.B., Lang, T., Krauss, M., Nagy, G., Haucke, V., Jahn, R., and Neher, E. (2005). Plasmalemmal phosphatidylinositol-4,5-bisphosphate level regulates the releasable vesicle pool size in chromaffin cells. J Neurosci *25*, 2557-2565. 10.1523/jneurosci.3761-04.2005.

Mohrmann, R., de Wit, H., Connell, E., Pinheiro, P.S., Leese, C., Bruns, D., Davletov, B., Verhage, M., and Sorensen, J.B. (2013). Synaptotagmin interaction with SNAP-25 governs vesicle docking, priming, and fusion triggering. J Neurosci *33*, 14417-14430. 10.1523/JNEUROSCI.1236-13.2013.

Mohrmann, R., de Wit, H., Verhage, M., Neher, E., and Sørensen, J.B. (2010). Fast vesicle fusion in living cells requires at least three SNARE complexes. Science (New York, N.Y.) *330*, 502-505. 10.1126/science.1193134.

Neher, E., and Brose, N. (2018). Dynamically Primed Synaptic Vesicle States: Key to Understand Synaptic Short-Term Plasticity. Neuron *100*, 1283-1291. 10.1016/j.neuron.2018.11.024.

Neher, E., and Sakaba, T. (2001). Combining deconvolution and noise analysis for the estimation of transmitter release rates at the calyx of held. J Neurosci *21*, 444-461. 10.1523/jneurosci.21-02-00444.2001.

Nishiki, T., and Augustine, G.J. (2004). Dual roles of the C2B domain of synaptotagmin I in synchronizing Ca2+-dependent neurotransmitter release. J Neurosci *24*, 8542-8550. 10.1523/JNEUROSCI.2545-04.2004.

Nyenhuis, S.B., Karandikar, N., Kiessling, V., Kreutzberger, A.J.B., Thapa, A., Liang, B., Tamm, L.K., and Cafiso, D.S. (2021). Conserved arginine residues in synaptotagmin 1 regulate fusion pore expansion through membrane contact. Nat Commun *12*, 761. 10.1038/s41467-021-21090-x.

Nyenhuis, S.B., Thapa, A., and Cafiso, D.S. (2019). Phosphatidylinositol 4,5 Bisphosphate Controls the cis and trans Interactions of Synaptotagmin 1. Biophysical journal *117*, 247-257. 10.1016/j.bpj.2019.06.016.

Paddock, B.E., Wang, Z., Biela, L.M., Chen, K., Getzy, M.D., Striegel, A., Richmond, J.E., Chapman, E.R., Featherstone, D.E., and Reist, N.E. (2011). Membrane penetration by synaptotagmin is required for coupling calcium binding to vesicle fusion in vivo. J Neurosci *31*, 2248-2257. 10.1523/JNEUROSCI.3153-09.2011.

Pérez-Lara, Á., Thapa, A., Nyenhuis, S.B., Nyenhuis, D.A., Halder, P., Tietzel, M., Tittmann, K., Cafiso, D.S., and Jahn, R. (2016). PtdInsP(2) and PtdSer cooperate to trap synaptotagmin-1 to the plasma membrane in the presence of calcium. Elife *5*. 10.7554/eLife.15886.

Quade, B., Camacho, M., Zhao, X., Orlando, M., Trimbuch, T., Xu, J., Li, W., Nicastro, D., Rosenmund, C., and Rizo, J. (2019). Membrane bridging by Munc13-1 is crucial for neurotransmitter release. Elife *8*. 10.7554/eLife.42806.

Radhakrishnan, A., Li, X., Grushin, K., Krishnakumar, S.S., Liu, J., and Rothman, J.E. (2021). Symmetrical arrangement of proteins under release-ready vesicles in presynaptic terminals. Proceedings of the National Academy of Sciences of the United States of America *118*. 10.1073/pnas.2024029118.

Radhakrishnan, A., Stein, A., Jahn, R., and Fasshauer, D. (2009). The Ca2+ affinity of synaptotagmin 1 is markedly increased by a specific interaction of its C2B domain with phosphatidylinositol 4,5-bisphosphate. The Journal of biological chemistry *284*, 25749-25760. 10.1074/jbc.M109.042499.

Rickman, C., and Davletov, B. (2003). Mechanism of calcium-independent synaptotagmin binding to target SNAREs. The Journal of biological chemistry *278*, 5501-5504. 10.1074/jbc.C200692200.

Rosenmund, C., Sigler, A., Augustin, I., Reim, K., Brose, N., and Rhee, J.S. (2002). Differential control of vesicle priming and short-term plasticity by Munc13 isoforms. Neuron *33*, 411-424. 10.1016/s0896-6273(02)00568-8.

Rothman, J.E., Krishnakumar, S.S., Grushin, K., and Pincet, F. (2017). Hypothesis - buttressed rings assemble, clamp, and release SNAREpins for synaptic transmission. FEBS Lett *591*, 3459-3480. 10.1002/1873-3468.12874.

Ruiter, M., Kádková, A., Scheutzow, A., Malsam, J., Söllner, T.H., and Sørensen, J.B. (2019). An Electrostatic Energy Barrier for SNARE-Dependent Spontaneous and Evoked Synaptic Transmission. Cell Rep *26*, 2340-2352.e2345. 10.1016/j.celrep.2019.01.103.

Schneggenburger, R., and Neher, E. (2000). Intracellular calcium dependence of transmitter release rates at a fast central synapse. Nature *406*, 889-893. 10.1038/35022702.

Schotten, S., Meijer, M., Walter, A.M., Huson, V., Mamer, L., Kalogreades, L., ter Veer, M., Ruiter, M., Brose, N., Rosenmund, C., et al. (2015). Additive effects on the energy barrier for synaptic vesicle fusion cause supralinear effects on the vesicle fusion rate. Elife *4*, e05531. 10.7554/eLife.05531.

Schupp, M., Malsam, J., Ruiter, M., Scheutzow, A., Wierda, K.D., Sollner, T.H., and Sorensen, J.B. (2016). Interactions Between SNAP-25 and Synaptotagmin-1 Are Involved in Vesicle Priming, Clamping Spontaneous and Stimulating Evoked Neurotransmission. J Neurosci *36*, 11865-11880. 10.1523/JNEUROSCI.1011-16.2016.

Seven, A.B., Brewer, K.D., Shi, L., Jiang, Q.X., and Rizo, J. (2013). Prevalent mechanism of membrane bridging by synaptotagmin-1. Proceedings of the National Academy of Sciences of the United States of America *110*, E3243-3252. 10.1073/pnas.1310327110.

Shao, X., Li, C., Fernandez, I., Zhang, X., Südhof, T.C., and Rizo, J. (1997). Synaptotagmin-syntaxin interaction: the C2 domain as a Ca2+-dependent electrostatic switch. Neuron *18*, 133-142. 10.1016/s0896-6273(01)80052-0.

Shi, L., Shen, Q.T., Kiel, A., Wang, J., Wang, H.W., Melia, T.J., Rothman, J.E., and Pincet, F. (2012). SNARE proteins: one to fuse and three to keep the nascent fusion pore open. Science (New York, N.Y.) *335*, 1355-1359. 10.1126/science.1214984.

Shin, O.H., Lu, J., Rhee, J.S., Tomchick, D.R., Pang, Z.P., Wojcik, S.M., Camacho-Perez, M., Brose, N., Machius, M., Rizo, J., et al. (2010). Munc13 C2B domain is an activity-dependent Ca2+ regulator of synaptic exocytosis. Nature structural & molecular biology *17*, 280-288. 10.1038/nsmb.1758.

Shin, O.H., Xu, J., Rizo, J., and Südhof, T.C. (2009). Differential but convergent functions of Ca2+ binding to synaptotagmin-1 C2 domains mediate neurotransmitter release. Proceedings of the National Academy of Sciences of the United States of America *106*, 16469-16474. 10.1073/pnas.0908798106.

Silva, M., Tran, V., and Marty, A. (2021). Calcium-dependent docking of synaptic vesicles. Trends Neurosci. 10.1016/j.tins.2021.04.003.

Sinha, R., Ahmed, S., Jahn, R., and Klingauf, J. (2011). Two synaptobrevin molecules are sufficient for vesicle fusion in central nervous system synapses. Proceedings of the National Academy of Sciences of the United States of America *108*, 14318-14323. 10.1073/pnas.1101818108.

Sørensen, J.B., Fernández-Chacón, R., Südhof, T.C., and Neher, E. (2003). Examining synaptotagmin 1 function in dense core vesicle exocytosis under direct control of Ca2+. J Gen Physiol *122*, 265-276. 10.1085/jgp.200308855.

Stevens, C.F., and Sullivan, J.M. (2003). The Synaptotagmin C2A Domain Is Part of the Calcium Sensor Controlling Fast Synaptic Transmission. Neuron *39*, 299-308. 10.1016/s0896-6273(03)00432-x.

Striegel, A.R., Biela, L.M., Evans, C.S., Wang, Z., Delehoy, J.B., Sutton, R.B., Chapman, E.R., and Reist, N.E. (2012). Calcium binding by synaptotagmin's C2A domain is an essential element of the electrostatic switch that triggers synchronous synaptic transmission. J Neurosci *32*, 1253-1260. 10.1523/jneurosci.4652-11.2012.

Sudhof, T.C. (2002). Synaptotagmins: why so many? The Journal of biological chemistry *277*, 7629-7632. 10.1074/jbc.R100052200.

Sudhof, T.C. (2013). Neurotransmitter release: the last millisecond in the life of a synaptic vesicle. Neuron *80*, 675-690. 10.1016/j.neuron.2013.10.022.

Sun, J., Pang, Z.P., Qin, D., Fahim, A.T., Adachi, R., and Sudhof, T.C. (2007). A dual-Ca2+-sensor model for neurotransmitter release in a central synapse. Nature *450*, 676-682. 10.1038/nature06308.

Takamori, S., Holt, M., Stenius, K., Lemke, E.A., Grønborg, M., Riedel, D., Urlaub, H., Schenck, S., Brügger, B., Ringler, P., et al. (2006). Molecular anatomy of a trafficking organelle. Cell *127*, 831-846. 10.1016/j.cell.2006.10.030.

Tang, J., Maximov, A., Shin, O.H., Dai, H., Rizo, J., and Südhof, T.C. (2006). A complexin/synaptotagmin 1 switch controls fast synaptic vesicle exocytosis. Cell *126*, 1175-1187. 10.1016/j.cell.2006.08.030.

Tawfik, B., Martins, J.S., Houy, S., Imig, C., Pinheiro, P.S., Wojcik, S.M., Brose, N., Cooper, B.H., and Sørensen, J.B. (2021). Synaptotagmin-7 places dense-core vesicles at the cell membrane to promote Munc13-2- and Ca(2+)-dependent priming. Elife *10*. 10.7554/eLife.64527.

van den Bogaart, G., Meyenberg, K., Diederichsen, U., and Jahn, R. (2012). Phosphatidylinositol 4,5-bisphosphate increases Ca2+ affinity of synaptotagmin-1 by 40-fold. The Journal of biological chemistry *287*, 16447-16453. 10.1074/jbc.M112.343418.

van den Bogaart, G., Meyenberg, K., Risselada, H.J., Amin, H., Willig, K.I., Hubrich, B.E., Dier, M., Hell, S.W., Grubmuller, H., Diederichsen, U., and Jahn, R. (2011a). Membrane protein sequestering by ionic protein-lipid interactions. Nature *479*, 552-555. 10.1038/nature10545.

van den Bogaart, G., Thutupalli, S., Risselada, J.H., Meyenberg, K., Holt, M., Riedel, D., Diederichsen, U., Herminghaus, S., Grubmuller, H., and Jahn, R. (2011b). Synaptotagmin-1 may be a distance regulator acting upstream of SNARE nucleation. Nature structural & molecular biology *18*, 805-812. 10.1038/nsmb.2061.

Verhage, M., and Sørensen, J.B. (2008). Vesicle docking in regulated exocytosis. Traffic (Copenhagen, Denmark) *9*, 1414-1424. 10.1111/j.1600-0854.2008.00759.x.

Voleti, R., Tomchick, D.R., Sudhof, T.C., and Rizo, J. (2017). Exceptionally tight membrane-binding may explain the key role of the synaptotagmin-7 C2A domain in asynchronous neurotransmitter release. Proceedings of the National Academy of Sciences of the United States of America *114*, E8518-E8527. 10.1073/pnas.1710708114.

Wang, L.Y., Neher, E., and Taschenberger, H. (2008). Synaptic vesicles in mature calyx of Held synapses sense higher nanodomain calcium concentrations during action potential-evoked glutamate release. J Neurosci *28*, 14450-14458. 10.1523/JNEUROSCI.4245-08.2008.

Wang, S., Li, Y., and Ma, C. (2016). Synaptotagmin-1 C2B domain interacts simultaneously with SNAREs and membranes to promote membrane fusion. Elife *5*. 10.7554/eLife.14211.

Wen, H., Linhoff, M.W., McGinley, M.J., Li, G.L., Corson, G.M., Mandel, G., and Brehm, P. (2010). Distinct roles for two synaptotagmin isoforms in synchronous and asynchronous transmitter release at zebrafish neuromuscular junction. Proceedings of the National Academy of Sciences of the United States of America *107*, 13906-13911. 10.1073/pnas.1008598107.

Wilhelm, B.G., Mandad, S., Truckenbrodt, S., Kröhnert, K., Schäfer, C., Rammner, B., Koo, S.J., Claßen, G.A., Krauss, M., Haucke, V., et al. (2014). Composition of isolated synaptic boutons reveals the amounts of vesicle trafficking proteins. Science (New York, N.Y.) *344*, 1023-1028. 10.1126/science.1252884.

Wolfel, M., Lou, X., and Schneggenburger, R. (2007). A mechanism intrinsic to the vesicle fusion machinery determines fast and slow transmitter release at a large CNS synapse. J Neurosci *27*, 3198-3210. 10.1523/JNEUROSCI.4471-06.2007.

Wölfel, M., and Schneggenburger, R. (2003). Presynaptic capacitance measurements and Ca2+ uncaging reveal submillisecond exocytosis kinetics and characterize the Ca2+ sensitivity of vesicle pool depletion at a fast CNS synapse. J Neurosci *23*, 7059-7068. 10.1523/jneurosci.23-18-07059.2003.

Wu, Z., Bello, O.D., Thiyagarajan, S., Auclair, S.M., Vennekate, W., Krishnakumar, S.S., O'Shaughnessy, B., and Karatekin, E. (2017). Dilation of fusion pores by crowding of SNARE proteins. Elife *6*. 10.7554/eLife.22964.

Wu, Z., Dharan, N., McDargh, Z.A., Thiyagarajan, S., O'Shaughnessy, B., and Karatekin, E. (2021a). The neuronal calcium sensor Synaptotagmin-1 and SNARE proteins cooperate to dilate fusion pores. Elife *10*. 10.7554/eLife.68215.

Wu, Z., Ma, L., Courtney, N.A., Zhu, J., Zhang, Y., Chapman, E.R., and Karatekin, E. (2021b). Polybasic patches in both C2 domains of Synaptotagmin-1 are required for evoked neurotransmitter release. bioRxiv, 2021.2007.2005.451149. 10.1101/2021.07.05.451149.

Xu, J., Mashimo, T., and Sudhof, T.C. (2007). Synaptotagmin-1, -2, and -9: Ca(2+) sensors for fast release that specify distinct presynaptic properties in subsets of neurons. Neuron *54*, 567-581. 10.1016/j.neuron.2007.05.004.

Xue, M., Ma, C., Craig, T.K., Rosenmund, C., and Rizo, J. (2008). The Janus-faced nature of the C(2)B domain is fundamental for synaptotagmin-1 function. Nature structural & molecular biology *15*, 1160-1168. 10.1038/nsmb.1508.

Yao, J., Gaffaney, J.D., Kwon, S.E., and Chapman, E.R. (2011). Doc2 is a Ca2+ sensor required for asynchronous neurotransmitter release. Cell *147*, 666-677. 10.1016/j.cell.2011.09.046.

1402 Zhou, Q., Lai, Y., Bacaj, T., Zhao, M., Lyubimov, A.Y., Uervirojnangkoorn, M., Zeldin, O.B., Brewster, A.S.,
1403 Sauter, N.K., Cohen, A.E., et al. (2015). Architecture of the synaptotagmin-SNARE machinery for
1404 neuronal exocytosis. Nature *525*, 62-67. 10.1038/nature14975.
1405 Zhou, Q., Zhou, P., Wang, A.L., Wu, D., Zhao, M., Sudhof, T.C., and Brunger, A.T. (2017). The primed
1406 SNARE-complexin-synaptotagmin complex for neuronal exocytosis. Nature *548*, 420-425.
1407 10.1038/nature23484.

1408

Supplementary figures

Figure 1 – Figure supplement 1

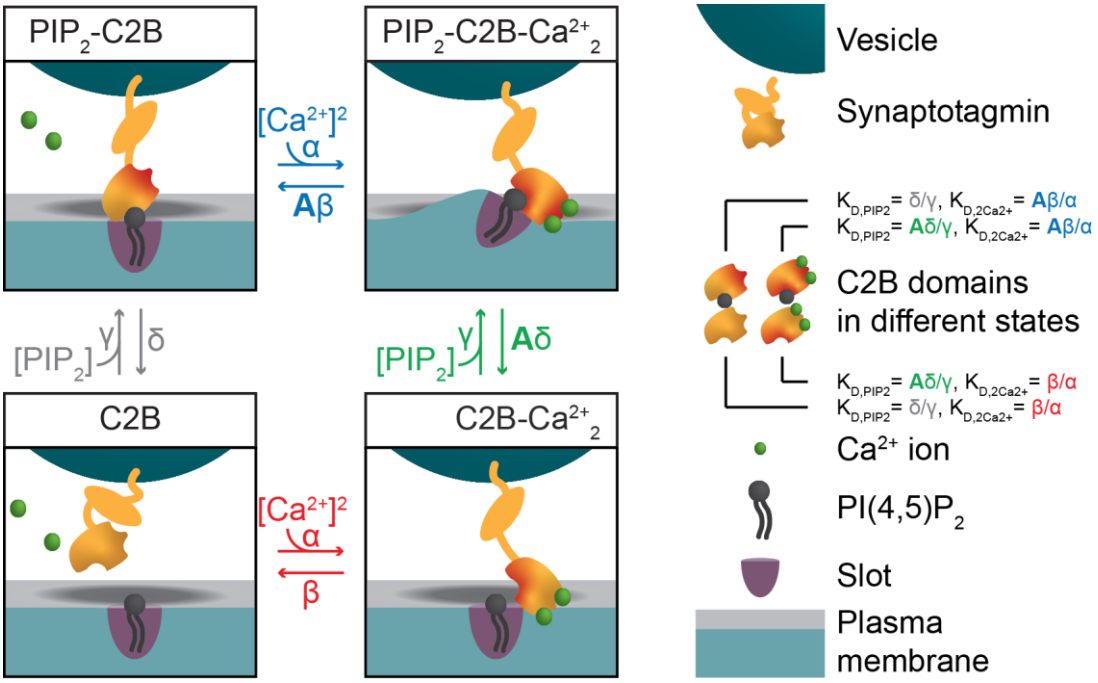

Figure 1 – figure supplement 1: Alternative reaction scheme of a single syt in which Ca^{2+} binding leads to association to the plasma membrane. Reaction scheme of a single syt C2B domain alternative to the one shown in Figure 1A. Instead of an association to the vesicular membrane, Ca^{2+} binding to the C2B domain in this illustration leads to an association with the plasma membrane. In this illustration, the dual-bound state affects the curvature of plasma membrane. Our model does not make a distinction between either of the two illustrations.

Figure 1 – figure supplement 2

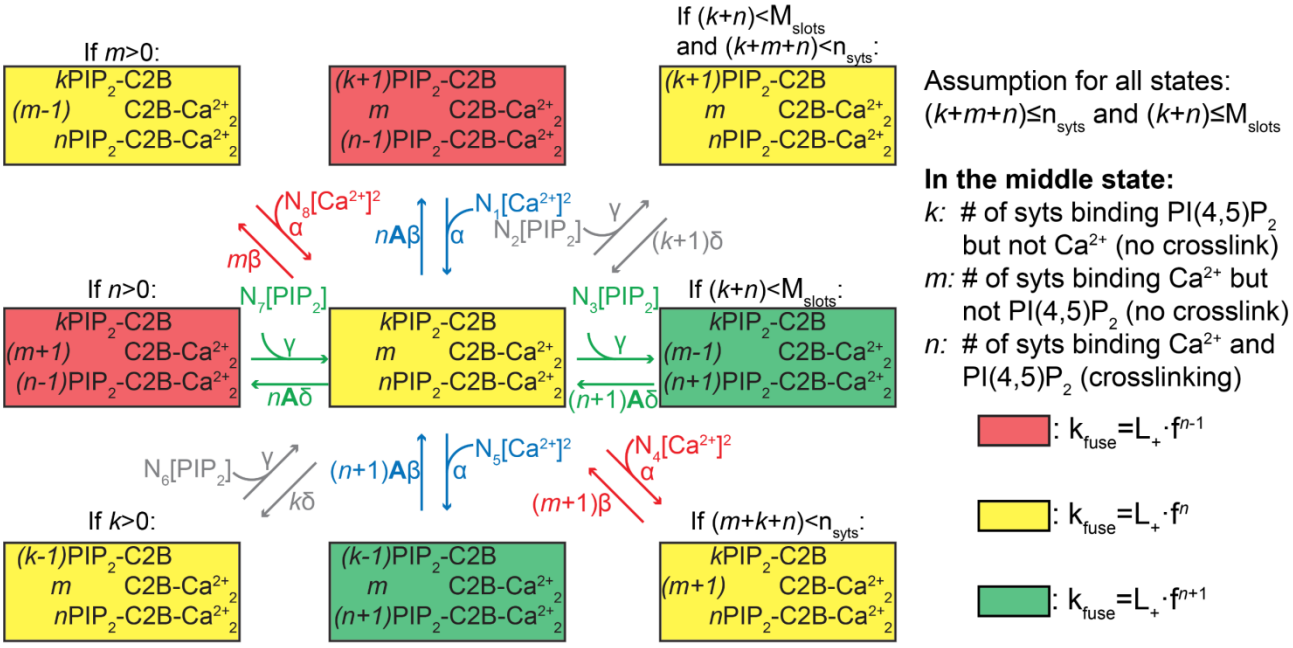

$N_1=k+1$; $N2=(n_{syts}-k-m-n)(M_{slots}-k-n)$; $N_3=m(M_{slots}-k-n)$; $N_4=(n_{syts}-k-m-n)$; $N_5=k$;

$N_6=(n_{syts}-(k-1)-m-n)(M_{slots}-(k-1)-n)$; $N_7=(m+1)(M_{slots}-k-(n-1))$; $N_8=(n_{syts}-k-(m-1)-n)$.

Figure 1 – figure supplement 2: Reaction scheme for all reactions of an entire SV. The diagram shows the possible (un)binding reactions and indicates the relative fusion rate of an SV with n_{syts} syts and M_{slots} slots. The state in the center of the diagram represents an SV with *k* syts having bound only PI(4,5)P_2, *m* syts having bound only two Ca^{2+}, and *n* syts having formed dual bindings by binding both PI(4,5)P_2 and two Ca^{2+}. From this state, the SV can (un)bind Ca^{2+} or PI(4,5)P_2 (unbinding moves the SV to the state to the left or up, binding to the right or down). The number of syts, n_{syts}, and the number of slots, M_{slots}, limit the possible number of syts engaging in ligand binding in general and in binding of PI(4,5)P_2, respectively, which is indicated by the assumption in the top right corner. Whether the SV can undergo a specific reaction (that is, whether a certain state exists and the SV can transit to it) depends on its current binding state as indicated by the assumptions above some of the states. The color shading of the states indicates the value of the fusion rate relative to the other states in the diagram. Yellow shading means a fusion rate equal to that from the state in the center. Red and green shading means a factor *f* lower and higher fusion rate, respectively. For detailed description of the reaction rate equations, see Methods.

1434 **Figure 2 – figure supplement 1**

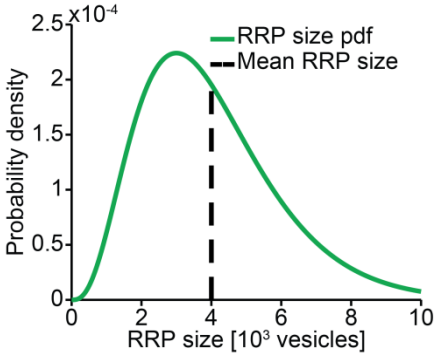

1435

1436 **Figure 2 – figure supplement 1: RRP distribution**. We assumed the RRP size to follow a gamma distribution with
1437 mean 4000 and SD 2000.

1438 **Figure 2 figure supplement 2**

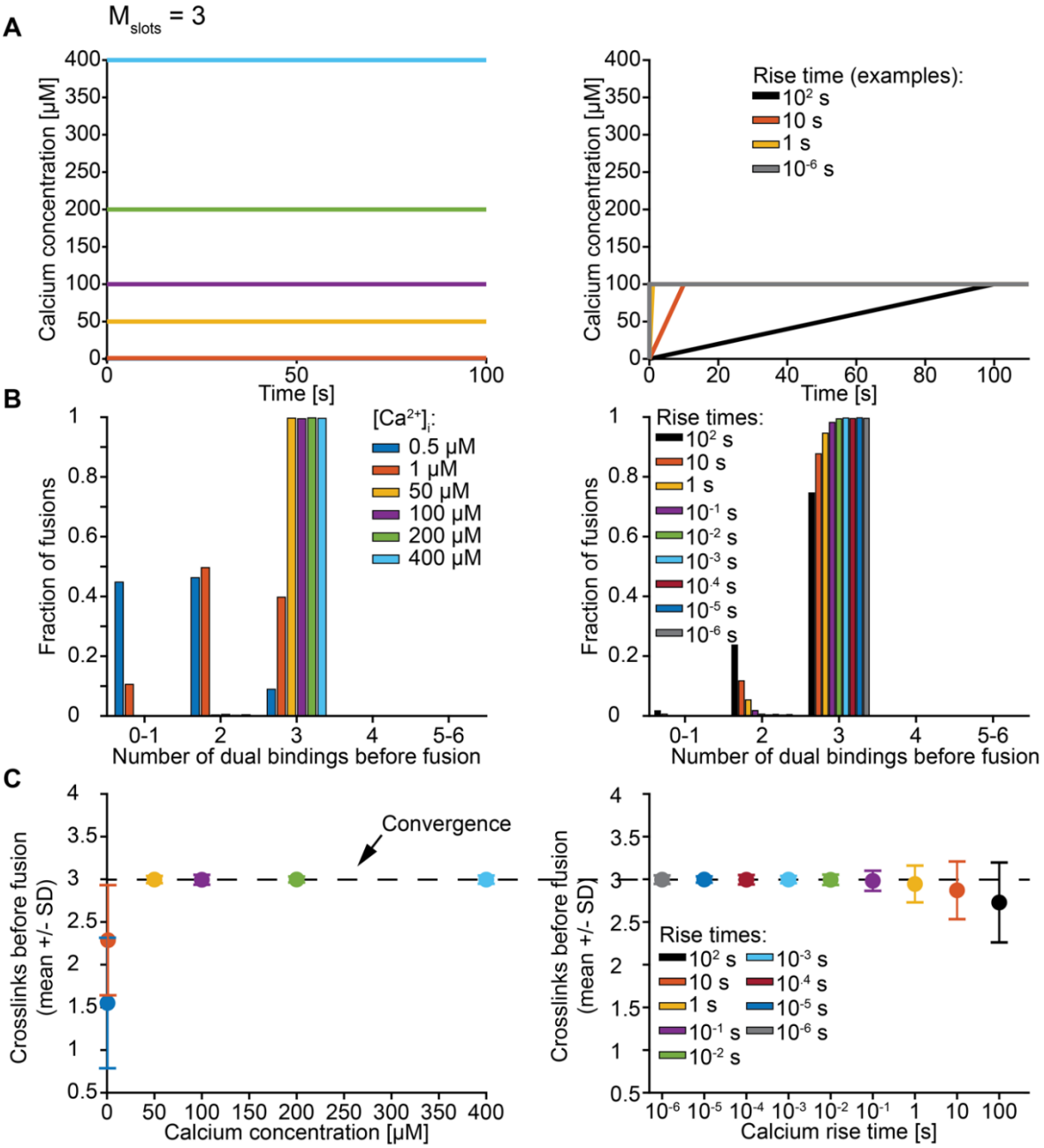

1439

1440 **Figure 2 – figure supplement 2: Exploration of the number of dual bindings formed before fusion of an SV with**
1441 **M_{slots}=3. A)** The Ca^{2+} signal used in simulations with step (left) and ramp (right) Ca^{2+} functions. In simulations with
1442 step Ca^{2+} the concentrations rises instantly at t=0 from the basal Ca^{2+} of 50 nM to various constant
1443 concentrations. In simulations with ramp Ca^{2+} the Ca^{2+} concentration increases linearly from the basal
1444 concentration of 50 nM to 100 µM Ca^{2+} with various rise times. **B)** The number of dual bindings formed before
1445 fusion for various Ca^{2+} concentrations (step Ca^{2+}, left) or Ca^{2+} rise times (ramp Ca^{2+}, right) as depicted in A. The
1446 bars show proportion of 10000 stochastically simulated SVs. The number of dual bindings formed before fusion
1447 increased with increasing step Ca^{2+} concentrations and decreasing Ca^{2+} rise times. At high concentrations or fast
1448 rise times, most fusions took place after forming 3 dual bindings. **C)** Average number of dual bindings formed
1449 before fusion in simulations of 10000 SVs with Ca^{2+} signals as depicted in A. The average number of dual bindings
1450 formed before fusion increases with increasing step Ca^{2+} concentration and decreases with increasing Ca^{2+} rise
1451 time. A plateau is reached at an average of 3 dual bindings at high step Ca^{2+} concentrations and low rise times.
1452 Error bars show ± standard deviation.

1453 **Figure 2 – figure supplement 3**

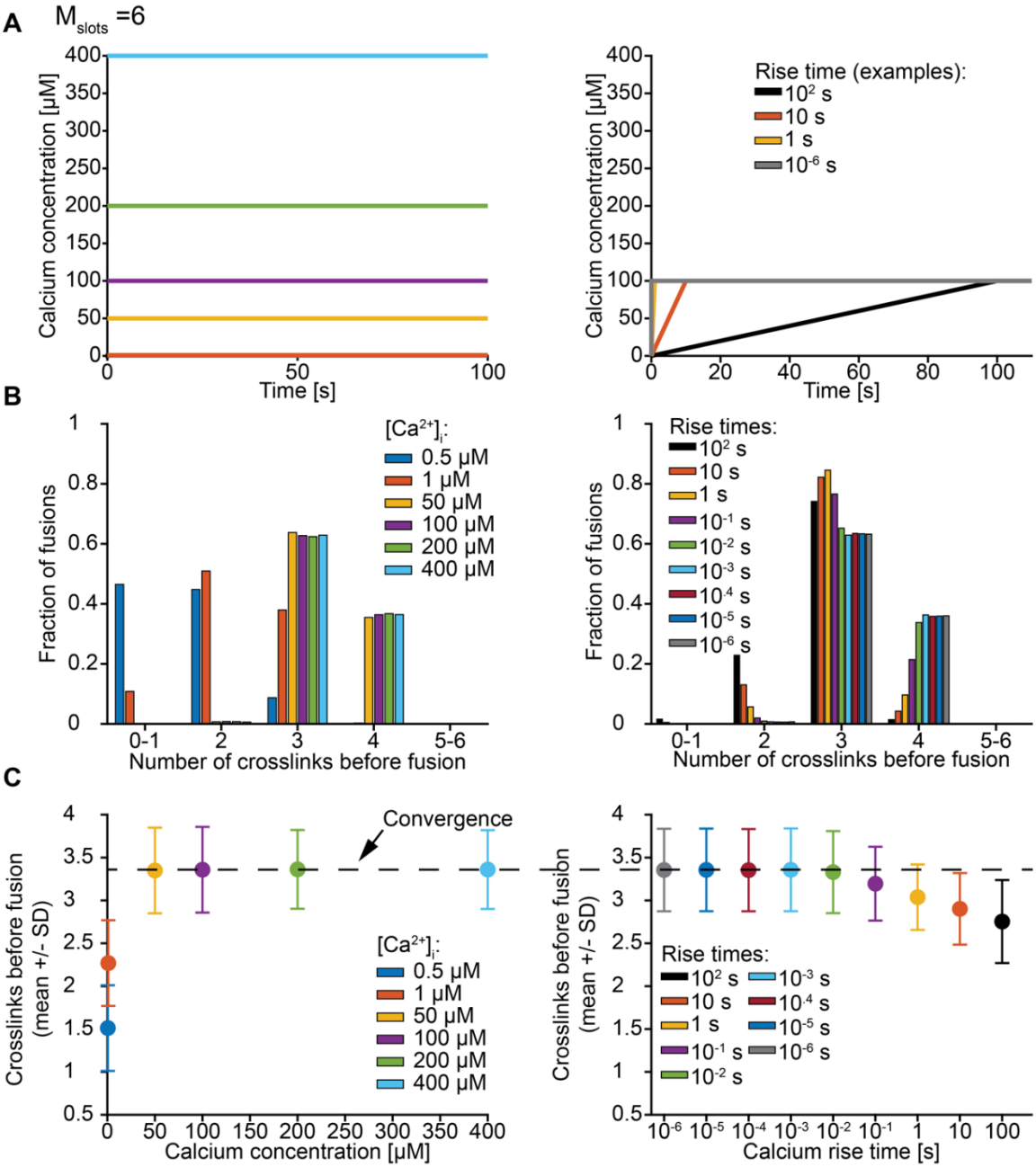

1454

1455 **Figure 2 – figure supplement 3: Exploration of the number of dual bindings formed before fusion of an SV with**
1456 **M_{slots}=6. A)** The Ca^{2+} signal used in simulations with step (left) and ramp (right) Ca^{2+} functions. In simulations with
1457 step Ca^{2+} the concentrations rises instantly at t=0 from the basal Ca^{2+} of 50 nM to various constant
1458 concentrations. In simulations with ramp Ca^{2+} the Ca^{2+} concentration increases linearly from the basal
1459 concentration of 50 nM to 100 µM Ca^{2+} with various rise times. **B)** The number of dual bindings formed before
1460 fusion for various Ca^{2+} concentrations (step Ca^{2+}, left) or Ca^{2+} rise times (ramp Ca^{2+}, right) as depicted in A. The
1461 bars show percentages of 10000 stochastically simulated SVs. The number of dual bindings formed before fusion
1462 increased with increasing step Ca^{2+} concentrations and decreasing Ca^{2+} rise times. At high concentrations or fast
1463 rise times, most fusions took place after forming 3-4 dual bindings. **C)** Average number of dual bindings formed
1464 before fusion in simulations of 10000 SVs with Ca^{2+} signals as depicted in A. The average number of dual bindings
1465 formed before fusion increases with increasing step Ca^{2+} concentration and decreases with increasing Ca^{2+} rise
1466 time. A plateau is reached at an average of 3.4 dual bindings at high step Ca^{2+} concentrations and low rise times.
1467 Error bars show ± standard deviation.

1468 **Figure 2 figure supplement 4**

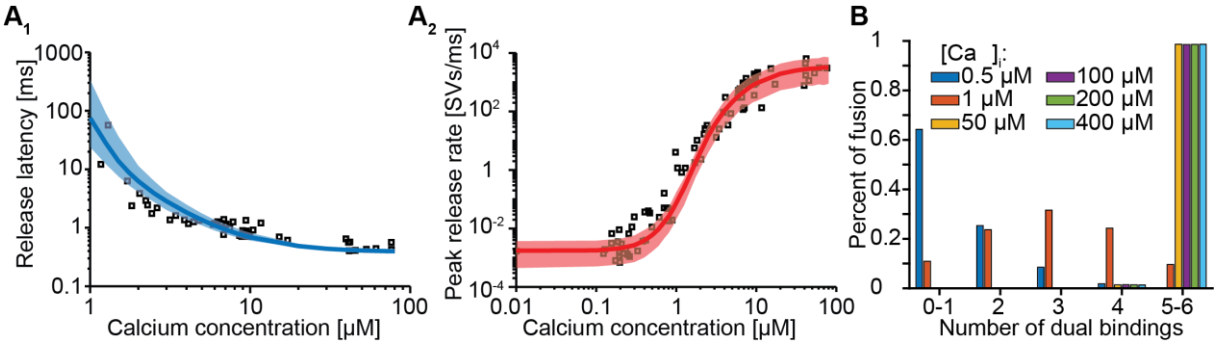

1469

1470 **Figure 2 – figure supplement 4: Forcing fusion from a state in which 5-6 syts are dual-binding Ca^{2+} and $PI(4,5)P_2$**
1471 **causes a too steep Ca^{2+} dependecy of the peak release rates. A)** Best fit results for a model with 6 slots forced
1472 to show most fusion events when 5/6 dual-bounds were formed. We achieved this by setting *f* to a fixed value
1473 of 12.79 (computed following: $f_{new} = (f_{initial})^{\frac{3}{6}}$, with $f_{initial}$ being the best fit value at M_{slots}=6 of $f_{initial}$: 163.5)
1474 and we only fitted the four remaining parameters. The best fit results show larger deviation from the
1475 experimantally obtained release latencies (A_1) and peak release rates (A_2) compared to the initial fit with (M_{slots}=6
1476 and *f* as a free parameter). Solid lines show median release latencies (A_1) and mean peak release rates (A_2)
1477 predicted by the model from 1000 repetitions per simulated $[Ca^{2+}]_i$. The shaded areas indicate the 95% prediction
1478 interval of the model. **B)** Number of dual bindings formed before fusion for various Ca^{2+} concentrations. The bars
1479 show the proportion of 10000 stochastically simulated SVs that fuse with a certain number of dual bounds
1480 formed. Most fusion events occur when 5-6 dual bounds have formed. Best fit parameters: α=22.96 $\mu M^{-2}s^{-1}$,
1481 γ=0.49 $\mu M^{-1}s^{-1}$, $[PI(4,5)P_2]$=12.71 µM, f=12.79 (fixed), d=0.3850 ms. Experimental data points in the figures are
1482 replotted from Kochubey and Schneggenburger (2011).

1483 **Figure 2 – figure supplement 5**

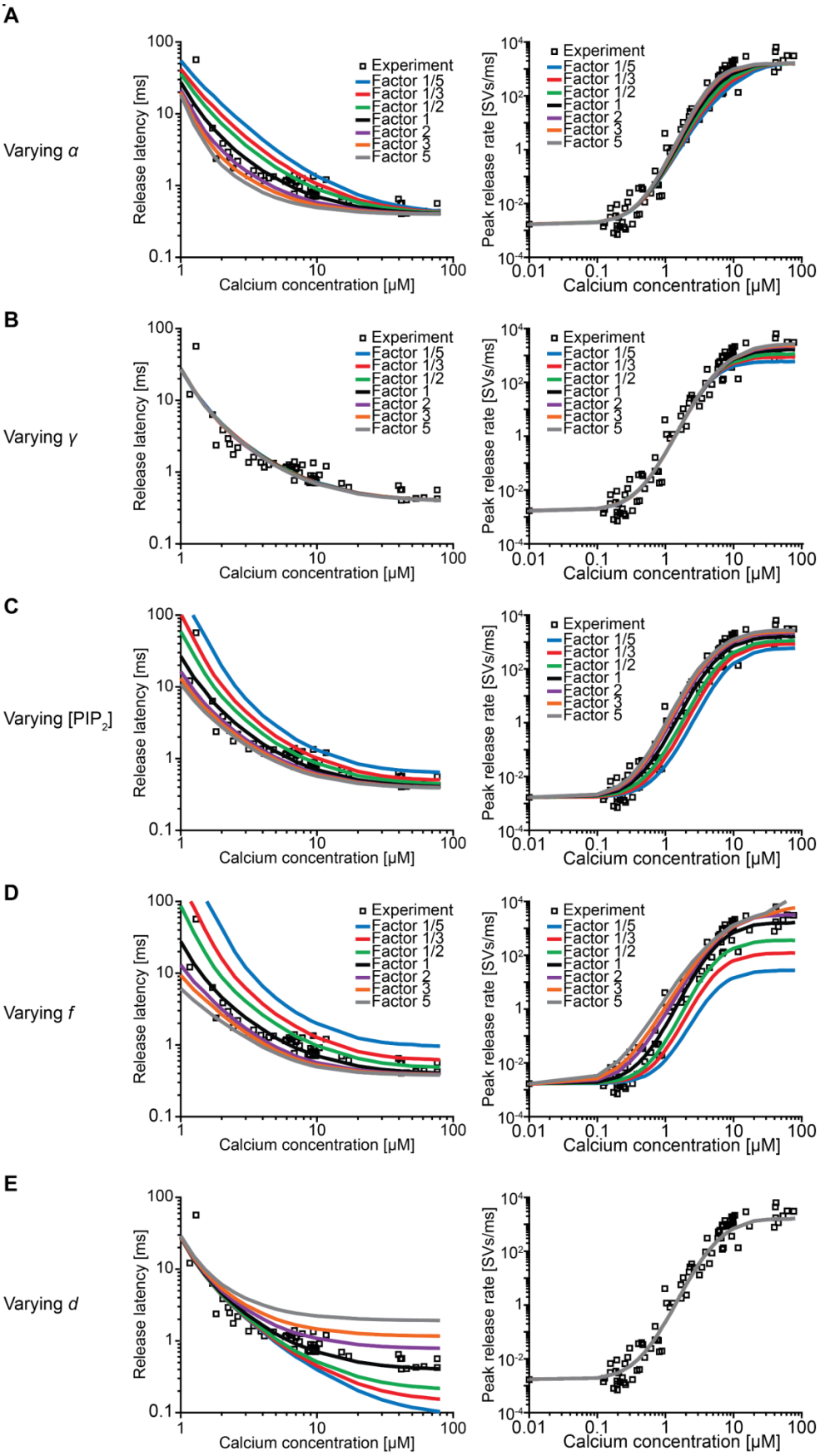

1484

1485 **Figure 2 – figure supplement 5: Effect of the free parameters on release latencies and peak release rates.**

A-E) Effect on release latencies (left) and peak release rates (right) when varying *α* (A), *γ* (B), [PI(4,5)P_2] (C), *f* (D), and *d* (E). The best-fit values of each of the parameters were increased and decreased by a factor 2, 3 and 5. Varying α and γ leads to a change in β and δ so that the measured affinities for both Ca^{2+} and PI(4,5)P_2 are still matched (van den Bogaart *et al.*, 2012). (**A)** When varying *α* the release latency is mostly affected in the middle range of $[Ca^{2+}]_i$. The effect on the peak release rates is very small **B)** Varying *γ* has no effect on release latencies. The effect of varying γ on peak release is larger at high $[Ca^{2+}]_i$ compared to low $[Ca^{2+}]_i$ reflecting that at high $[Ca^{2+}]_i$ PI(4,5)P_2 binding limits dual binding formation. **C)** Varying [PI(4,5)P_2] has a large effect on the release latencies and peak release rates. The effect of varying [PI(4,5)P_2] is much larger compared to varying γ, as changing [PI(4,5)P_2] only affects the binding rate of PI(4,5)P_2, whereas changing γ leads to an equal change in δ to match the published affinity values. Furthermore [PI(4,5)P_2] affects the steady state distribution. **D)** Varying *f* has a large effect on both release latency and fusion rate, as it directly impacts the effect of dual binding formation on SV fusion rates. **E)** Varying the added delay, *d*, only shifts the release latencies linearly and does not affect the peak release rates. Experimental data points in these figures are replotted from Kochubey and Schneggenburger (Kochubey and Schneggenburger, 2011).

1500 **Figure 3 – figure supplement 1**

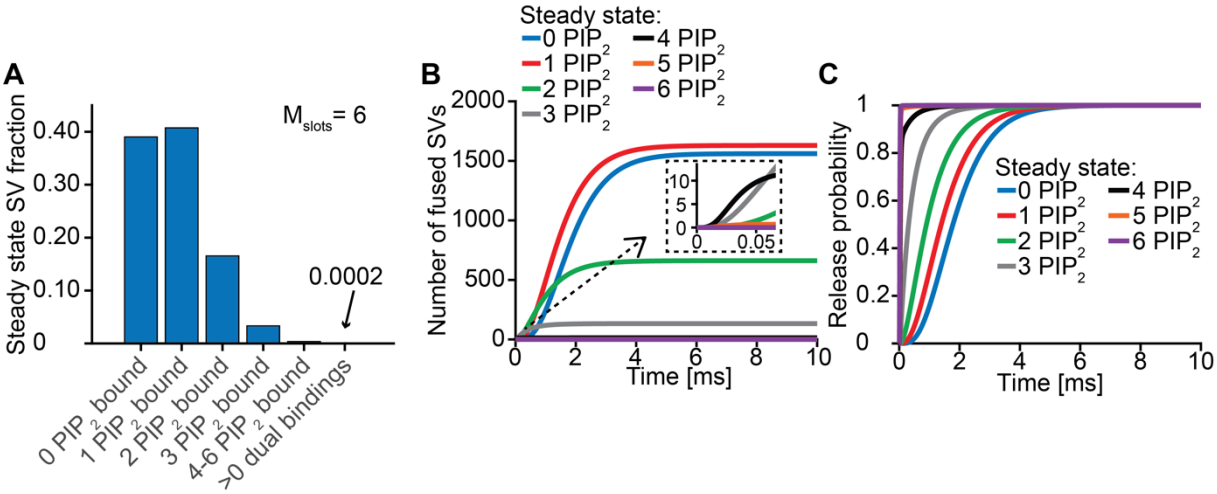

1501
1502 **Figure 3 – figure supplement 1. Syt-binding to PI(4,5)P_2 prior to Ca^{2+} stimulus underlies very fast SV fusion**
1503 **(model with M_{slots}=6). A)** PI(4,5)P_2 binding status of SVs at steady state. At resting $[Ca^{2+}]_i$ of 50 nM, more than 40
1504 % of SVs have bound a single PI(4,5)P_2 molecule (not including those that have formed a dual binding), more than
1505 15 % has bound two PI(4,5)P_2, while less than 5 % has bound three PI(4,5)P_2. Very few SVs have bound more than
1506 3 PI(4,5)P_2 and almost no SVs form dual bindings at steady state. **B)** Cumulative fusion of SVs after 50 µM step
1507 Ca^{2+} at t=0, grouped according to their initial PI(4,5)P_2 binding state. During the first ~0.5 ms, release is dominated
1508 by SVs having two or three syts bound to PI(4,5)P_2 prior to the stimulus. The zoom-in shows that the SVs having
1509 three or four syts prebound to PI(4,5)P_2 constitute the majority of release of the first five SVs and therefore
1510 determines the release latency. **C)** Cumulative release probability over time of SVs after 50 µM step Ca^{2+} at t=0,
1511 grouped according to initial PI(4,5)P_2 binding state. The dominance of SVs having pre-bound to PI(4,5)P_2 with two
1512 to four syts in panel B is explained by their high release probability compared to SVs with no or only one PI(4,5)P_2
1513 bound.

1514 **Figure 4 – figure supplement 1**

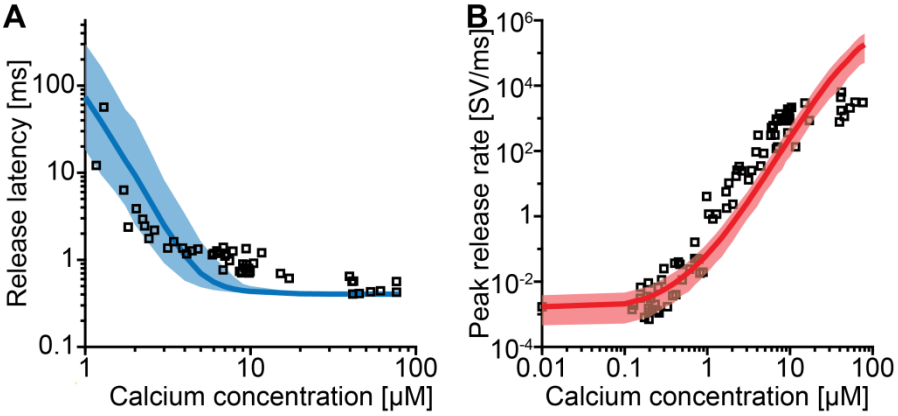

1515

1516

1517 **Figure 4 – figure supplement 1: Fitting of the model without allosteric interaction between Ca^{2+} and PI(4,5)P_2**
1518 **fails to reproduce the Ca^{2+}-dependency of NT release. A-B)** The best fit results for a model with 3 slots and no
1519 allosteric interaction between Ca^{2+} and PI(4,5)P_2 (A=1). In A the median release latency and the 95% prediction
1520 interval of the best fit model are shown. Note that the y-axis range is different from Figure 2A, but the
1521 proportions of the ticks is maintained to help comparison. B) The mean maximal fusion rate as a function of
1522 $[Ca^{2+}]_i$ and the corresponding 95% prediction interval. Best fit parameters used to generate these curves are:
1523 α=2.174 $\mu M^{-2}s^{-1}$, γ=6.773·10^5 $\mu M^{-1}s^{-1}$, [PI(4,5)P_2]=2991 μM, f=3.943·10^5, d=0.4036 ms. Experimental data points
1524 in the figures are replotted from Kochubey and Schneggenburger (2011). Similar to the best fit solutions with too
1525 few slots (Figure 2A, left), the fitted *f* value was extremely high, which forced quick SV fusion before the newly
1526 formed dual binding dissolved. Thus, when assuming realistic affinities for Ca^{2+} and PI(4,5)P_2, the allosteric
1527 property of the syt C2B domain, which leads to a stabilization of the dual-bound state, is necessary to ensure
1528 high Ca^{2+} sensitivity of release.

1529

1530

1531 **Figure 5 – Figure supplement 1**

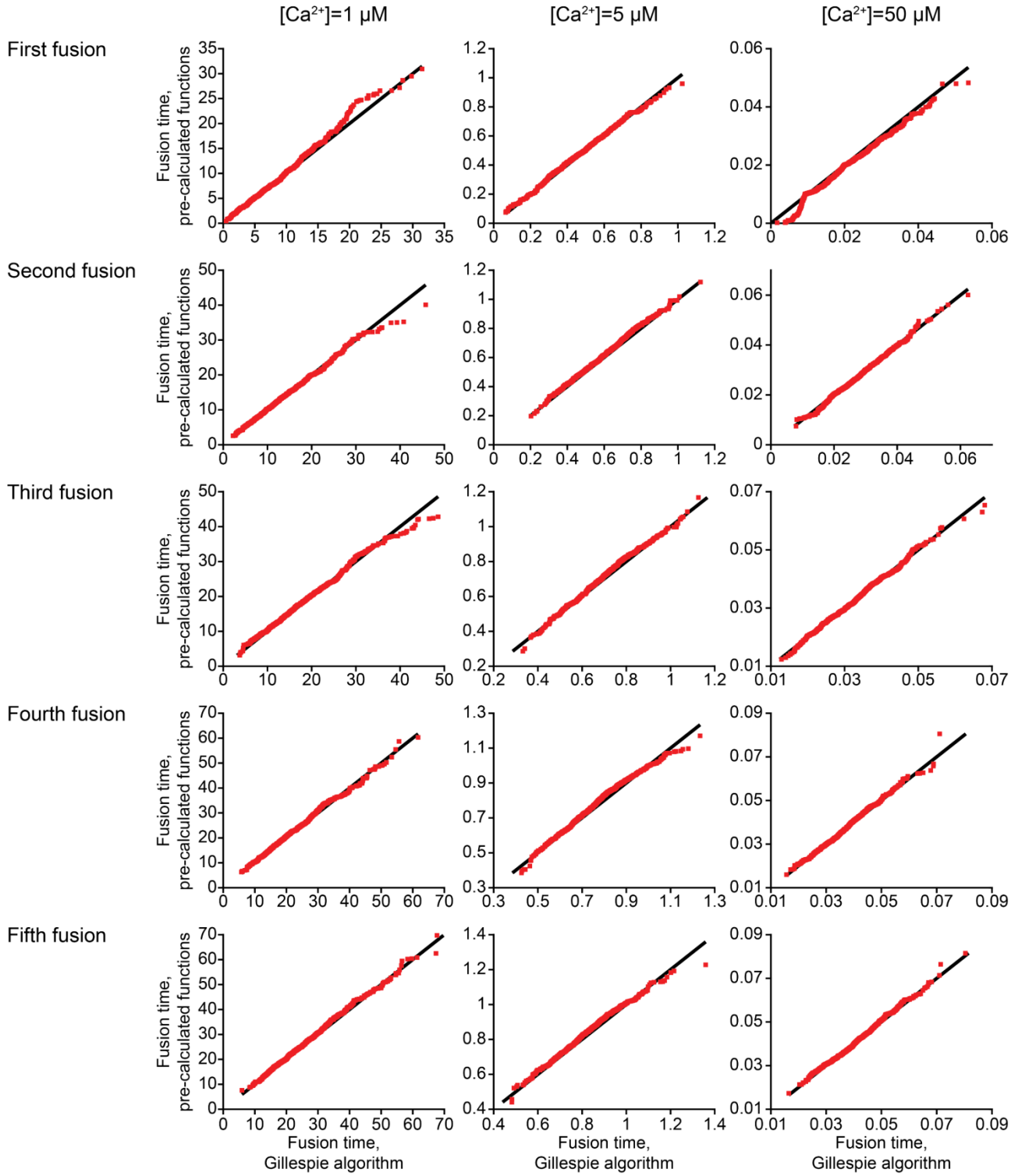

1532

1533 **Figure 5 – Figure supplement 1: Comparing the two different model implementations.** QQ-plots comparing the
1534 first five fusion times obtained using stochastic simulations with an implementation based on the closed-form
1535 solution of the model and using the Gillespie algorithm for three different $[Ca^{2+}]_i$ (see Methods). Black line
1536 respresent 1:1 correspondence, which would only happen in deterministic simulations. Red squares indicate
1537 fusion time simulated with both methods for 1000 repetitions.

1538

1539 **Figure 5 – figure supplement 2**

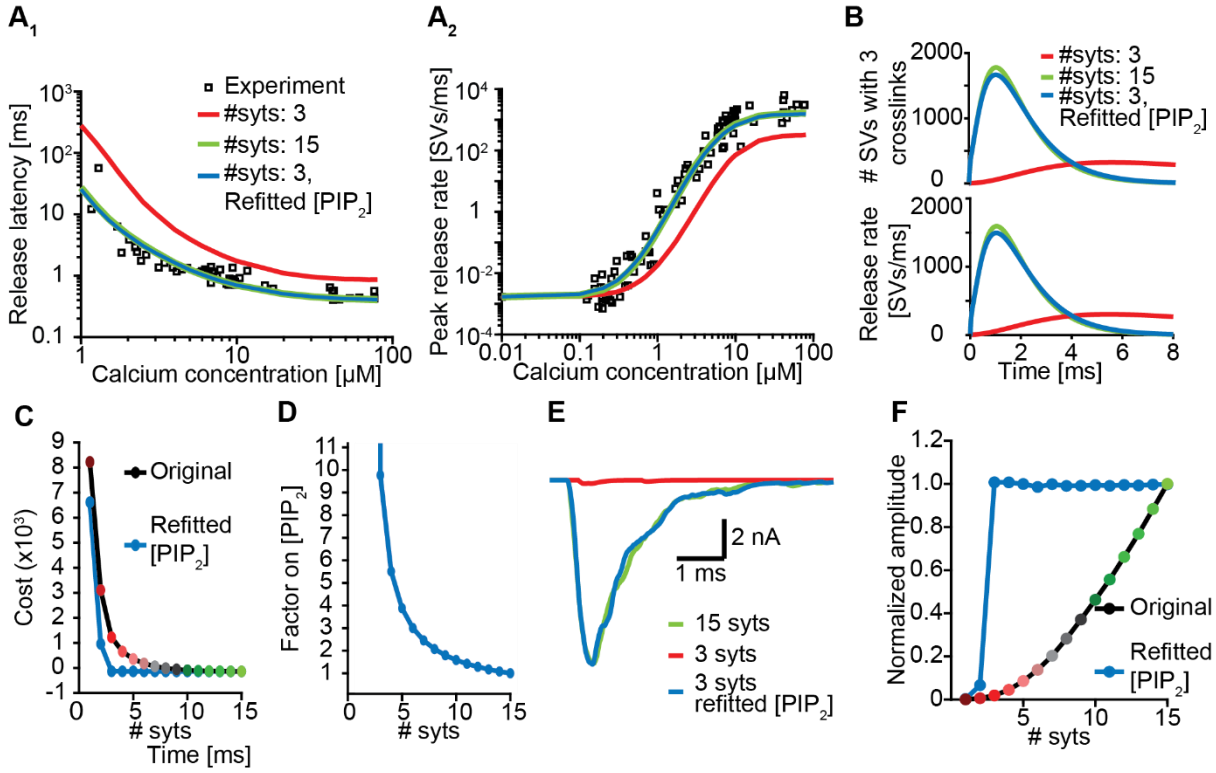

1540

1541

1542 **Figure 5 – figure supplement 2. Upregulation of PI(4,5)P_2 can compensate for loss of syts A)** Release latencies
1543 (A_1) and peak release rates (A_2) for a model with 15 syts (green) and with 3 syts before (red) and after (blue)
1544 refitting of [PI(4,5)P_2]. Experimental data points in panels A are replotted from Kochubey and Schneggenburger
1545 (2011).**B)** The average number of SVs with three dual bindings formed (top) and the corresponding release rates
1546 (bottom) as a function of time upon stimulation with a Ca^{2+}-flash of 50 µM for a model with 15 syts (green), and
1547 with 3 syts before (red) and after (blue) refitting of [PI(4,5)P_2]. **C)** The costs values associated with the Ca^{2+}-
1548 uncaging data for different levels of syt with the original best fit parameters (black line) and after re-fitting
1549 [PI(4,5)P_2] for each choice of n_{syts} (blue line). **D)** The fold-increase in [PI(4,5)P_2] obtained by re-fitting the model
1550 as a function of the number of syts**. E)** Representative AP-evoked response of a model with 3 syts per SV obtained
1551 after increasing [PI(4,5)P_2] plotted together with representative responses for a model with 3 and 15 syts with
1552 the original [PI(4,5)P_2]. **F)** Average amplitudes of simulated AP-evoked responses at original [PI(4,5)P_2] and using
1553 the increased values.

1554

1555

1556 **Figure 6 – figure supplement 1**

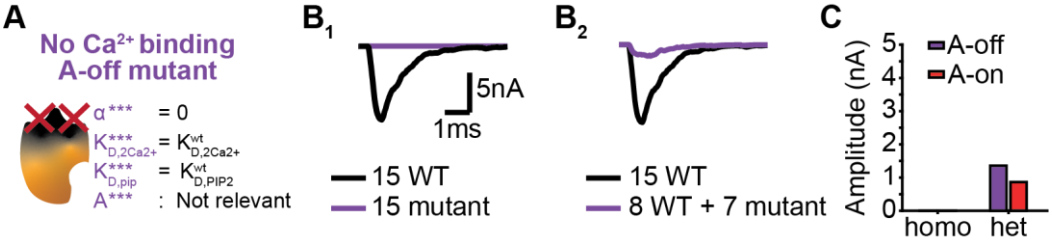

1557

1558 **Figure 6 – figure supplement 1. The dominant negative effect of a mutant that is unable to bind Ca^{2+} depend**
1559 **on the mutants $PI(4,5)P_2$ affinity. A)** Schematic illustration of the "*No Ca^{2+}-binding, A-off*" mutant, which is not
1560 able to bind Ca^{2+} implying that the allosteric interaction between Ca^{2+} and $PI(4,5)P_2$ is always 'inactive'. **B)**
1561 Representative, stochastically simulated AP-responses with homozygous (left, 15 mutants) and heterozygous
1562 (right, 7 mutants + 8 WT) of the A-off mutant. For each of the examples representative trace of a condition with
1563 15 WT syts is shown in black. **C)** Comparison of the mean amplitudes of AP-evoked responses (n=200) simulated
1564 with "*No Ca^{2+}-binding, A-off*" mutant to the mean amplitudes of the "*No Ca^{2+}-binding, A-on*" mutant (Figure 6).

1565

1566 **Table 1. Fixed parameters in the model**

Parameter	Description	Value	Reference
n_{syts}	Number of syts per SV	15	(Takamori *et al.*, 2006)
M_{slots}	Number of binding slots for syt to $PI(4,5)P_2$ (see Figure 2)	Varied from 1-6	This paper
n_{ves}	Number of RRP vesicles	Mean: 4000, sd: 2000, gamma distribution	(Wölfel and Schneggenburger, 2003)
$[Ca^{2+}]_0$	Resting $[Ca^{2+}]_i$	0.05 µM	(Helmchen et al., 1997)
$K_{D,2Ca2+}$	Dissociation constant of C2B for two Ca^{2+} ions	221^2 μM^2	(van den Bogaart *et al.*, 2012)
$K_{D,PIP2}$	Dissociation constant of C2B for $PI(4,5)P_2$	20 µM	(van den Bogaart *et al.*, 2012)
A	Allosteric factor see Methods for calculation	0.00022	(van den Bogaart *et al.*, 2012)
β	Ca^{2+} unbinding rate constant	$K_{D,2Ca2+} \cdot \alpha$	Computed using best fit α (see Table 2)
δ	$PI(4,5)P_2$ unbinding rate constant of C2B	$K_{D,PIP2} \cdot \gamma$	Computed using best fit α (see Table 2)
L_+	Basal fusion rate	$4.23 \cdot 10^{-4}\ s^{-1}$	Computed using data from (Kochubey and Schneggenburger, 2011)

1567

1568

1569 **Table 2. Best fit model parameters and corresponding costs with different number of slots**

Parameter	Description	M_{slots} =1	M_{slots} =2	M_{slots} =3	M_{slots} =4	M_{slots} =5	M_{slots} =6
α ($\mu M^{-2}s^{-1}$)	Ca^{2+} association rate constant	0.03712	34.99	24.70	25.08	24.51	24.11
γ ($\mu M^{-1}s^{-1}$)	$PI(4,5)P_2$ association rate constant	$1.425 \cdot 10^5$	572.6	124.7	121.3	124.31	126.6
$[PI(4,5)P_2]$ (μM)	Effective $PI(4,5)P_2$ concentration for syt	0.009658	0.2523	1.109	0.4528	0.3048	0.2320
f (E_{syt} (K_bT))	Factor on the release rate for each $Ca^{2+}/PI(4,5)P_2$ dual bound C2B domain (resulting from a fusion barrier reduction of E_{syt})	$4.259 \cdot 10^6$ (15.3)	1298 (7.17)	128.2 (4.85)	152.1 (5.02)	159.6 (5.07)	163.5 (5.10)
d (ms)	Added delay	0.3211	0.3761	0.3803	0.3866	0.3876	0.3881
Costs	Quantification of goodness of fit	581.9	-92.50	-139.4	-130.3	-127.7	-126.5

1570

1571

1572 **Table 3. Overview of possible reactions and their rates in the model**

Reaction	Condition	Triplet notation	Reaction rate
Binding of PI(4,5)P_2 to empty syt	$n+m+k<n_{syts}$ and $n+k<M_{slots}$	*(n,m,k)->(n,m,k+1)*	$(n_{syts}-n-m-k)(M_{slots}-n-k)[PI(4,5)P_2]\gamma$
Unbinding of PI(4,5)P_2	$k>0$	*(n,m,k->(n,m,k-1)*	$k\delta$
Binding of $Ca^{2+}{}_2$ to empty syt	$n+m+k<n_{syts}$	*(n,m,k)->(n,m+1,k)*	$(n_{syts}-n-m-k)[Ca^{2+}]^2\alpha$
Unbinding of $Ca^{2+}{}_2$	$m>0$	*(n,m,k)->(n,m-1,k)*	$m\beta$
Binding of PI(4,5)P_2 to form dual binding	$n+k<M_{slots}$ and $m>0$	*(n,m,k)->(n+1,m-1,k)*	$m(M_{slots}-n-k)[PI(4,5)P_2]\gamma$
Unbinding of PI(4,5)P_2 from a dual binding	$n>0$	*(n,m,k)->(n-1, m+1,k)*	$An\delta$
Binding of $Ca^{2+}{}_2$ to form a dual binding	$k>0$	*(n,m,k)->(n+1,m,k-1)*	$k[Ca^{2+}]^2\alpha$
Unbinding of $Ca^{2+}{}_2$ from a dual binding	n>0	*(n,m,k)->(n-1,m,k+1)*	$An\beta$
Fusion		*(n,m,k)->(F)*	$L_+ \cdot f^n$

1573